Water Table and Permeability Estimation From Multi-Channel Seismoelectric Spectral Ratios

Kaiyan Hu, Hengxin Ren, Qinghua Huang, Ling Zeng, Karl E Butler, Damien Jougnot, Niklas Linde, Klaus Holliger

Water Table and Permeability Estimation from Multi-Channel Seismoelectric Spectral Ratios

Kaiyan Hu[1,2,4], Hengxin Ren[3,4*], Qinghua Huang[1*], Ling Zeng[4], Karl E. Butler[5], Damien Jougnot[6], Niklas Linde[7], Klaus Holliger[7]

[1]Department of Geophysics, School of Earth and Space Sciences, Peking University, Beijing 100871, China.

[2]Shenzhen Institute, Peking University, Shenzhen 518057, China.

[3]Guangdong Provincial Key Laboratory of Geophysical High-resolution Imaging Technology, Southern University of Science and Technology, Shenzhen 518055, China.

[4]Department of Earth and Space Sciences, Southern University of Science and Technology, Shenzhen 518055, China.

[5]Department of Earth Sciences, University of New Brunswick, P.O. Box 4400, Fredericton, New Brunswick E3B 5A3, Canada.

[6]Sorbonne Université, CNRS, EPHE, UMR 7619 METIS, Paris F-75005, France.

[7]Institute of Earth Sciences, University of Lausanne, CH-1015 Lausanne, Switzerland.

Corresponding author: Qinghua Huang (huangq@pku.edu.cn); Hengxin Ren (renhx@sustech.edu.cn)

Key Points:

- Multi-channel seismoelectric spectral ratios are sensitive to the water table depth and the permeabilities of shallow layers
- Broad learning neural network is introduced to perform the inversion efficiently
- This study allows us to monitor the water table depth from the ground surface for an otherwise pre-defined model

Manuscript published in Journal of Geophysical Research: Solid Earth

Hu, K., Ren, H., Huang, Q., Zeng, L., Butler, K. E., Jougnot, D., Linde, N., Holliger, K. (2023) Water Table and Permeability Estimation from Multi-Channel Seismoelectric Spectral Ratios, Journal of Geophysical Research: Solid Earth, 128(5), e2022JB025505, doi:10.1029/2022JB025505.

Abstract

Recent developments in predicting and interpreting seismoelectric signals suggest a great potential for studying near-surface hydrogeological properties, particularly in the vadose zone. Previous studies have revealed that the seismoelectric spectral ratios obtained from earthquake-triggered seismoelectric data contain valuable hydrogeological information concerning porous media (e.g., permeability, porosity, fluid viscosity, and salinity). This study introduces Multi-Channel SeismoElectric Spectral Ratios (MC-SESRs) by considering an active seismic source acting on the ground surface. The frequency- and saturation-dependent excess charge density is adopted to calculate the cross-coupling coefficients. Applying a supervised learning task based on a flat neural network, the so-called "broad learning" model, to map and extract the features of MC-SESRs data, we seek to determine the permeability and the water table depth. Our results indicate that (1) MC-SESRs are sensitive to the water table depth and permeability; (2) using more traces of SESRs data for inversion can increase accuracy; (3) the changing water table can be rapidly determined by the MC-SESRs by resorting to the broad learning inverse model, and it can attain an excellent accuracy while disturbed by data noise and misspecified model parameters (e.g., porosity and permeability) with errors of up to 20%. The proposed MC-SESRs inversion has potential applications for non-invasive monitoring in shallow porous media (e.g., frost thawing and geothermal upwelling).

Plain Language Summary

A seismic source acting on the ground or occurring in porous materials containing water will generate seismic and electromagnetic field waves. The spectral ratios between the electric field and the seismic field are defined as SeismoElectric Spectral Ratios (SESRs), which are sensitive to physical properties' contrasts at layer boundaries (e.g., water table and hydrogeological and/or lithological layer boundaries). Applying SESRs to reconstruct hydrogeological parameters eliminates the need to know the seismic source function, which greatly facilitates quantitative interpretation. However, SESRs are often acquired by natural earthquakes in previous studies. It limits interpreting SESRs to one-trace data. This study uses an active seismic source to obtain the Multi-Channel SESRs (MC-SESRs). We conduct several experiments on synthetic MC-SESRs data by using a neural network to obtain water table depths and permeabilities for a layered Earth model. Our results show that the trained neural network can instantly predict the time-variant water table depths accurately. This study indicates that the quantitative interpretation of MC-SESRs data

allows for effective and rapid characterization of near-surface hydrogeological properties and also provide a possible approach for the non-invasive monitoring of hydrogeological variations in shallow porous media by using controllable source.

Keywords Hydrogeophysics; Seismoelectric coupling; Vadose zone; Water table monitoring; Seismoelectric spectral ratios; Broad learning

1. Introduction

In porous media, the surface of the solid grains (e.g., silicate minerals) is typically negatively charged due to fluid-mineral interactions (Glover & Jackson, 2010; Hunter, 1981; Revil et al., 2015). Considering the electrical double layer (EDL) model at the microscopic scale (1 - 10 nm) (Figure 1a), a portion of the counterions (cations for negatively charged mineral surfaces) coats the interface between the mineral surface and pore fluid forming the Stern layer while the remaining excess charges are distributed in the diffuse Gouy-Chapman layer (Glover & Jackson, 2010; Revil & Jardani, 2013). There is a shear plane in the diffuse Gouy-Chapman layer, beyond which the pore fluid and ions can move relative to the solid frame. As shown in Figure 1b, the electrical potential at the shear plane is defined as the Zeta potential (Hunter, 1981; Jougnot et al., 2020). The Zeta potential is commonly used to estimate the electrokinetic coupling coefficient, which characterizes the relationship between electrical and hydraulic potential differences associated with fluid flow within a porous medium (Hunter, 1981). Note that all acronyms used in this paper are listed in Table A1 of Appendix A.

Relative motions occur during the passage of seismic wavefields. Due to the electrokinetic effect, this process may generate streaming currents and natural electric fields (Pride, 1994; Revil et al., 2015; Revil & Linde, 2006). This process is commonly called seismoelectric (SE) conversion. The SE signals contain valuable information concerning the physical properties of both the pore fluid and the solid skeleton. The SE method can be used to determine hydrogeological properties provided the data measured on the ground surface or in boreholes are properly interpreted (Revil et al., 2012). During the past two decades, the SE method has seen significant development through (1) theoretical studies (e.g., Huang, 2002; Jougnot & Solazzi, 2021; Monachesi et al., 2018; Solazzi et al., 2022; Thanh et al., 2022), (2) numerical modeling approaches (e.g., Garambois & Dietrich, 2002; Grobbe & Slob, 2016; Haines & Pride, 2006; Hu

& Gao et al., 2011; Jougnot et al., 2013; Ren et al., 2016a, b; Zheng et al., 2021), (3) physical laboratory experiments (e.g., Bordes et al., 2015; Devis et al., 2018; Wang et al., 2020; Zhu & Toksöz, 2013), and (4) field measurements (e.g., Butler et al., 2018; Dupuis & Butler, 2006; Garambois & Dietrich, 2001; Rabbel et al., 2020; Thompson & Gist, 1993). As the understanding of SE signals grows, this method is of increasing interest to researchers in near-surface geophysics (e.g., Grobbe et al., 2020). The electromagnetic (EM) wave fields originating from seismic excitations are regarded as a superposition of three types of patterns (Figure 1c): (1) localized SE field waves accompanying seismic waves in porous media, which are also commonly referred to as coseismic electric field waves (Bordes et al., 2015; Jougnot et al., 2013; Pride & Garambois, 2002); (2) radiation waves induced on interfaces or directly converted from a seismic source (Dupuis et al., 2007; Haartsen & Pride, 1997; Garambois & Dietrich, 2002; Pride & Haartsen, 1996) and (3) evanescent waves generated on interfaces if the seismic incident angle is larger than the critical angle (Butler et al., 2018; Dzieran et al., 2019; Ren et al., 2016a; Yuan et al., 2021; Zheng et al., 2021). The generation of interfacial radiation and evanescent SE waves results from property contrasts at an interface (Garambois & Dietrich, 2002; Ren et al. 2016a, b). Interfacial radiation SE waves and evanescent SE waves offer a way to examine permeability or porosity contrasts (Dzieran et al., 2019, 2020), parameters determining the soil moisture characteristic (Zyserman et al., 2017), strong saturation contrasts such as the water table (Bordes et al., 2015; Warden et al., 2013), and other parameters (e.g., Archie's parameters, density, bulk, and shear modulus).

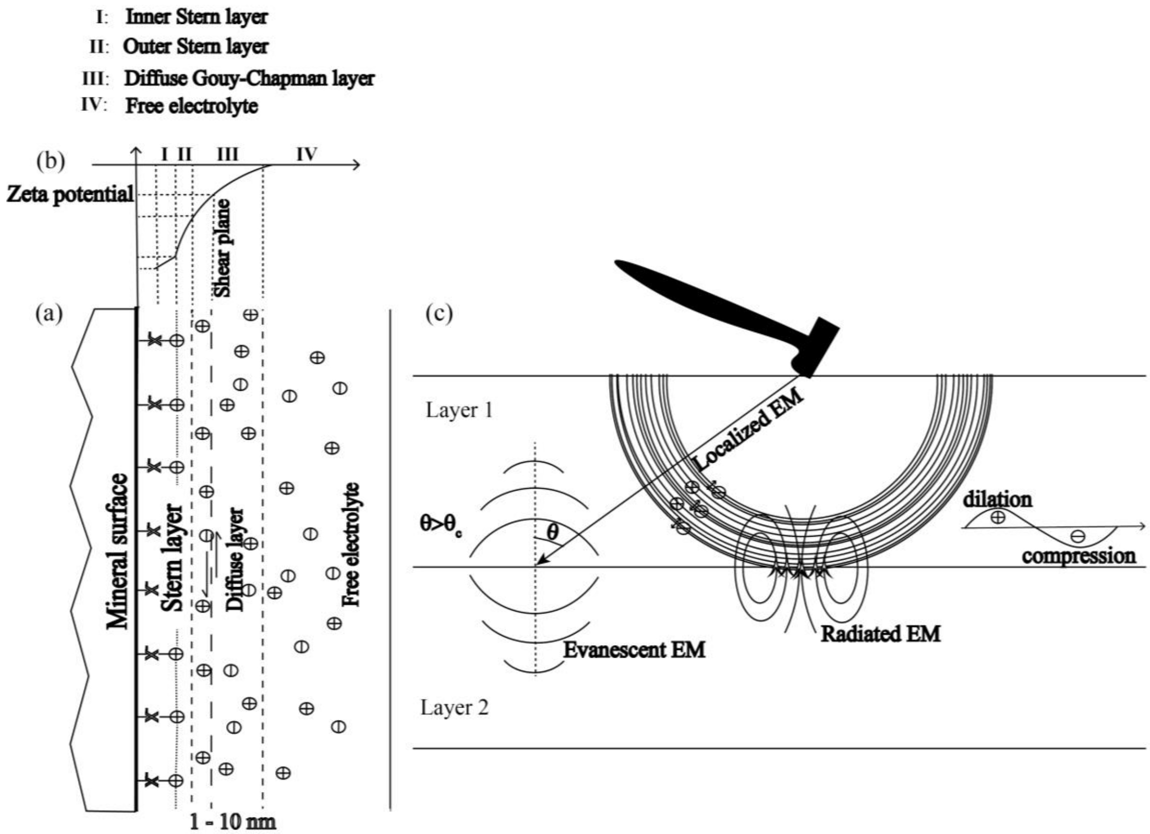

Figure 1. Schematic illustration of the generation of electromagnetic waves by seismoelectric conversion. (a) and (b) Electrical double layer and the corresponding electrical potential distribution. (c) Generation of localized, interfacial radiated, and evanescent electromagnetic wavefields due to an active seismic source.

Based on numerical simulation studies, Ren et al. (2016b) put forward the idea that evanescent SE waves could be the main contribution to EM signals observed during earthquakes. This idea was later adopted by Dzieran et al. (2019) to investigate earthquake-triggered SE signals in data from Northern Chile. They show that the SeismoElectric Spectral Ratios (SESRs), defined as the ratios between the absolute values of the electric field and the seismic acceleration in the frequency domain, have a site-specific frequency dependence with a decreasing amplitude with increasing frequency. Dzieran et al. (2019) explain this trend by the fact that the amplitudes of evanescent SE waves decay approximately with $\exp(-\omega p \Delta z)$, where ω is the angular frequency, p is the EM wave slowness, and Δz is the separation in depth between the receiver and the interface (Ren et al. 2018). Dzieran et al. (2019, 2020) successfully apply the SESRs to interpret shallow layered porous media's porosity and fluid salinity. However, Dzieran et al. (2020) state that the

SESRs are less sensitive to permeability variations. Inspired by Dzieran et al. (2019, 2020), this study extends the applications of SESRs data in several ways.

First, we change the strategy of calculating the SE coupling coefficient. Dzieran et al. (2019, 2020) calculate the electrokinetic coupling coefficient defined by Pride (1994), accounting for the Zeta potential. Instead, we rely on the effective excess charge density to calculate the electrokinetic coupling coefficient (e.g., Revil & Mahardika, 2013; Revil et al., 2015). Both in saturated and partially-saturated conditions, the effective excess charge density is highly correlated with permeability (Guarracino & Jougnot, 2018; Jougnot et al., 2020; Soldi et al., 2019). At low frequencies, the ratio of the effective excess charge density at partial water saturation to the excess charge density at full saturation is proportional to the reciprocal of water saturation under the assumption of a thick EDL model (Linde et al., 2007a; Revil et al., 2007). To account for frequency dependence, we adopt an approximate empirical formulation by using the relaxation time to relate the quasi-static to dynamic electrokinetic coupling coefficient proposed by Revil & Mahardika (2013), which has been tested by experimental measurements and other approaches (Jougnot & Solazzi, 2021).

Second, we consider the case of having both the seismic source and sensors located near the ground surface, which is very common in active-source SE field measurements (e.g., Butler et al., 1996, 2018; Dupuis et al., 2007; Garambois & Dietrich, 2001; Mikhailov et al., 1997; Thompson & Gist, 1993). Three-dimensional SE forward modeling algorithms using the reflectivity method (e.g., Garambois & Dietrich, 2002; Grobbe & Slob, 2016; Haartsen & Pride, 1997; Ren et al., 2007, 2010) to calculate full waveform simulations for layered media suffer from highly time-consuming computations when the source and receivers both lie very close to surface. As the computation of full waveforms relies on numerical integration in the wavenumber domain, the integrand oscillates strongly with the wavenumber when the depth difference between the source and the receiver is small, which may cause a slow convergence. Zheng et al. (2021) solved this convergence problem by adopting the peak-trough averaging method (Zhang et al., 2001, 2003), which selects peak and trough values in a stably oscillating sequence to apply the repeated average method (Dahlquist & Björck, 1974). Hence it offers an accurate and efficient tool for active-source SE forward modeling. This allows us to deal with any source-receiver geometries, particularly ground-based seismic sources. The Amplitude Variation versus Offset (AVO) method based on multi-channel observation has been widely applied in oil and gas exploration (Rutherford

& Williams, 1989). Multi-channel measurements can also be implemented in SE field experiments for stratified sediments. For example, Butler et al. (2018) presented that the multi-channel high-resolution EM field data, illustrating multiple modes of SE signals, providing information on subsurface porous materials complementary to that provided by multi-channel seismic reflection data. Moreover, Rabbel et al. (2020) document the potential of using the interfacial SE responses to map the water table by comparing the multi-channel SE measurements with other geophysical measurements, such as ground-penetrating radar and traditional seismic recordings. Inspired by AVO and SESRs, we propose a Multi-Channel SESRs (MC-SESRs) method that, in addition to frequency variations, makes use of the variations of SESRs with respect to the source-receiver offsets. Thus, we can use more spatial information of SESRs data in the inversions and obtain an improved reconstruction accuracy.

Third, the SESRs are determined by different parameters in different complicated non-linear ways. For example, the water table variations affect the water saturation distribution, which determines the effective permeability (e.g., Mualem, 1976; van Genuchten, 1980), the permittivity (e.g., Linde et al., 2006), the electrical conductivity, the electrokinetic coupling coefficient (e.g., Warden et al., 2013; Revil & Mahardika, 2013; Zyserman et al., 2017), the bulk density, the elastic moduli, the seismic velocity (e.g., Mao et al., 2022; Solazzi et al., 2021) and so on. Dzieran et al. (2019) mentioned that inverse modeling of SESRs may need a more advanced approach compared to the conventional linearized inversion algorithm used in their work. Machine learning, which is enjoying increasing interest in geophysics, may offer a corresponding option.

In this study, we rely on the broad learning (BL) model to invert hydrological parameters using MC-SESRs data. The BL system proposed by Chen and Liu (2017) is a flat neural network with a single lateral layer neural network, in contrast to deep structured neural networks. It is developed from the Random Vector Functional Link Neural Network (RVFLNN) (Pao et al., 1994) to apply an enhancement layer to link the input and output. Broadly expanding the enhancement nodes may enhance the capacity to approach non-linear problems. It only needs to learn the matrix weights of the link between the enhancement layer and output. Other matrix weights are randomly generated. Thus, the RVFLNN is a flat net without hidden layers, which avoids overtraining the neural network with many adjustable hyperparameters (Pao et al., 1994). Correspondingly, the BL structure improves the RVFLNN by adding a mapping feature layer to replace the original input based on the sparse autoencoder. Hence the BL structure first captures the features of input data in the mapping feature layer. Since the BL network structure is fixed, its main advantage is that it avoids elusive complicated deep architectures and iterative training processes (Gong et al., 2022). Its efficient capacities for processing noisy time series and text classifications have been verified (Chen & Liu, 2017; Du et al., 2020; Feng et al., 2019; Gong et al., 2022).

Most recently, Yang et al. (2022, 2023) applied the BL neural network to Rayleigh wave inversion. Considering a 1-D Earth model, Yang et al. (2022) examined the thickness and shear-wave velocity ranges of each layer by the well-trained BL neural network. Then they used the optimal ranges as the search space of a Bayesian approach to complement the parameter optimization. Their results indicated that this two-stage approach can provide more accurate shear-wave velocity models than without using a priori search space estimated by a BL model. Yang et al. (2023) also verified that using the BL approach to Rayleigh wave inversion may achieve a comparable accuracy but consume less training time than deep convolutional neural networks. In this study, we aim to determine hydrogeological parameters (water table depth and shallow layer permeabilities) under partially-saturated conditions by MC-SESRs data. For a specific investigated area whose layered structure had been determined, the well-trained BL model can, if fed with MC-SESR data, estimate the water table depth and update the permeability in the shallow layer in a quasi-instantaneous manner. Due to its high training efficiency, BL can easily be retrained to optimize the network when more MC-SESRs data is obtained. This study may provide a new monitoring strategy for obtaining the water table depths using the time-lapse MC-SESRs data. It also has the potential application in long-term observations for assessing groundwater storage and monitoring volcanic activities.

This paper is structured as follows. Section 2 describes the basic SE coupling equations, numerical simulation of the SE data, and our inversion framework. Section 3 focuses on analyzing the sensitivity of permeability and depth of water table (dwt) to MC-SESRs. Section 4 tests the performance of the BL neural network and presents the inversion results. Section 5 discusses the inversion results, and we provide conclusions in Section 6.

2. Methodology

2.1. Cross-coupling equations

For fluid-saturated isotropic porous media, the cross-coupled constitutive transport equations, including macroscopic Ohm's and Darcy's Law, can be expressed in the frequency domain through the following governing equations (Pride, 1994; Pride & Haartsen, 1996; Revil & Mahardika, 2013):

$$\mathbf{J} = \sigma^*(\omega)\mathbf{E} + L^*(\omega)(-\boldsymbol{\nabla} p_\mathrm{f} + \omega^2\rho_\mathrm{f}\mathbf{u}_\mathrm{s}), \tag{1}$$

$$-i\omega\mathbf{w} = L^*(\omega)\mathbf{E} + \frac{k^*(\omega)}{\eta_\mathrm{w}}(-\boldsymbol{\nabla} p_\mathrm{f} + \omega^2\rho_\mathrm{f}\mathbf{u}_\mathrm{s}), \tag{2}$$

$$-p_\mathrm{f} = C\nabla\cdot\mathbf{u}_\mathrm{s} + M\nabla\cdot\mathbf{w}, \tag{3}$$

$$\mathbf{T} = \left[\left(K_\mathrm{G} - \frac{2}{3}G\right)\nabla\cdot\mathbf{u}_\mathrm{s} + C\nabla\cdot\mathbf{w}\right]\mathbf{I} + G(\nabla\mathbf{u}_\mathrm{s} + \nabla{\mathbf{u}_\mathrm{s}}^\mathrm{T}), \tag{4}$$

$$-\rho_b\omega^2\mathbf{u}_\mathrm{s} - \rho_\mathrm{f}\omega^2\,\mathbf{w} = \left(K_G + \frac{4}{3}G\right)\nabla(\nabla\cdot\mathbf{u}_\mathrm{s}) - G\nabla\times\nabla\times\mathbf{u}_\mathrm{s} + C\nabla(\nabla\cdot\mathbf{w}) + \mathbf{F}, \tag{5}$$

where Equations 1-2 describe the electrokinetic cross-coupling relationship between the electric field $\mathbf{E}$ (V/m) and the volume-averaged fluid filtration displacement $\mathbf{w}$ (m) $= \phi(\mathbf{u}_\mathrm{f} - \mathbf{u}_\mathrm{s})$, which is defined by the porosity ϕ (m^3/m^3) and the volume-averaged fluid and solid displacements ($\mathbf{u}_\mathrm{f}$ and $\mathbf{u}_\mathrm{s}$). The subscripts 'f' and 's' designate fluid and solid properties, respectively. We consider a time-harmonic disturbance varying as $e^{-i\omega t}$ with $i = \sqrt{-1}$ the imaginary unit, $\omega = 2\pi f$ the angular frequency in rad/s, and f (Hz) the frequency. The superscript '*' indicates that a property is frequency-dependent and hence complex. $k^*(\omega)$ thus denotes the frequency-dependent permeability (m^2). Permeability reflects the ability of porous media to allow fluid to flow through the pores. Equations 3 and 4 describe the poroelastic relations (Biot, 1956, 1962a, b) with **I** denoting the identity matrix. The parameters C (Pa) and M (Pa) are associated with the elastic moduli (Pride, 1994). K_G (Pa) and G (Pa) denote the undrained bulk modulus and shear modulus of the solid skeleton. ρ_b (kg/m^3) and $\mathbf{F}$ (N) in Equation 5 are the mass density of the porous material and the body force applied on the bulk material, respectively. All parameters and their units used in this study are listed in Table A2 of Appendix A.

Due to harmonic variations of the bulk-stress tensor $\mathbf{T}$ (N/m^2) and the pore fluid pressure p_f (Pa), the flow changes from the viscous laminar regime to the inertial laminar regime beyond the critical or transition frequency (Revil & Mahardika, 2013; Solazzi et al., 2020, 2022). The permeability becomes frequency-dependent and complex-valued beyond the critical frequency, and its absolute value decreases with increasing frequency (Solazzi et al., 2020). η_w denotes the dynamic viscosity of pore water (1.002×10^{-3}Pa· s). The macroscopic electrical current density $\mathbf{J}$ (A/m^2) is the superposition of the conduction current density $\sigma^*(\omega)\mathbf{E}$ and the streaming current density $\mathbf{J}_\mathrm{ek}^*$ written by:

$$\mathbf{J}_\mathrm{ek}^* = L^*(\omega)(-\nabla p_\mathrm{f} + \omega^2 \rho_\mathrm{f} \mathbf{u}_\mathrm{s}), \tag{6}$$

in which $\sigma^*(\omega)$, and $\rho_\mathrm{f} = (1 - S_\mathrm{w})\rho_\mathrm{a} + \rho_\mathrm{w}$ denote the complex electrical conductivity (S/m) and the fluid density (kg/m^3), respectively. S_w, $\rho_\mathrm{a} = 1.21$ (kg/m^3) and $\rho_\mathrm{w} = 1000$ (kg/m^3) are the water saturation, the density of the air and pore water. Note that we consider pore water as a dilute solution with low salinities (commonly around 0.002 mol/L) and, hence, the solute density is neglected. For highly saline solutions (e.g., seawater, contaminated water), the mass density of the solute would need to be included. Unless mentioned otherwise, the parameters used in this paper refer to standard ambient conditions (1 atm and 20 ℃). The presence of harmonic electric fields usually makes the electrical conductivity of porous materials vary with frequency due to polarization effects of electrically conductive mineral grains, interfacial electrochemistry, or colloidal chemistry (Revil, 2013). The effective electrical conductivity in the frequency domain can be expressed by (Revil et al., 2015):

$$\sigma^*(\omega, S_\mathrm{w}) = F^{-1} S_\mathrm{w}^n \sigma_\mathrm{w} + \sigma_\mathrm{sur} + i\left(\sigma_\mathrm{quad} - \omega \varepsilon_0 \kappa\right). \tag{7}$$

Therein, n denotes the saturation exponent and $F = \phi^{-m}$ is the electrical formation factor in Archie's first and second laws with cementation exponent m (Archie, 1942). $\varepsilon_0 = 8.85418 \times 10^{-12}$ F/m is the vacuum permittivity. κ denotes the static effective dielectric constant, which is the function of the water saturation: (Linde et al., 2006):

$$\kappa(S_{\mathrm{w}}) = \frac{(F-1)\kappa_{\mathrm{s}} + {S_{\mathrm{w}}}^{n}\kappa_{\mathrm{w}} + (1-{S_{\mathrm{w}}}^{n})\kappa_{\mathrm{a}}}{F}. \tag{8}$$

The range of the dielectric constant for most rock-forming minerals is 4-6 and is commonly assumed to be $\kappa_{\mathrm{s}} = 4$ for dry sand grains in near-surface measurements (e.g., Fitterman, 2015; Knight & Endres, 2005). $\kappa_{\mathrm{w}} = 80.1$ and $\kappa_{\mathrm{a}} = 1$ represent the dielectric constants of the pore water and the air, respectively. Based on a volume-averaging method, Equation 8 is derived from a two-phase model (i.e. pore fluid and solid grains) by Pride (1994), accounting for the effective pore fluid formed by water and air and combining Archie's first and second laws (Linde et al., 2006). This equation assumes that the two fluid phases in the pore space are immiscible. The physical relationship (Equation 8) has been previously used to simulate seismoelectric signals (e.g., Rosas-Carbajal et al., 2020). The surface electrical conductivity σ_{sur} and the quadrature electrical conductivity σ_{quad} in Equation 7 are related to the fraction and mobility of counterions in the diffuse layer and in the Stern layer, respectively (Revil, 2013; Revil et al., 2015). Both conductivities are functions of water saturation. More details of these coefficients calculated by material properties and saturation levels, can be found in Table A3 of Appendix A.

Based on the EDL model (Figure 1a), Equations 1 and 2 express that the poromechanical influence contributes to the streaming source current, and the electric field contributes to the pore-fluid flow under the electroosmosis effect (Revil & Mahardika, 2013). The critical dynamic parameter $L^{*}(\omega)$ reflects the cross-coupling relationship. Due to the significance of frequency-dependent cross-coupling coefficient $L^{*}(\omega)$ in transport equations, its calculation has attracted considerable attention in the recent decade (Jougnot & Solazzi, 2021; Jouniaux & Zyserman, 2016; Soldi et al., 2020; Thanh et al., 2022; Warden et al., 2013). A popular approach is using the Zeta potential to describe the cross-coupling coefficient (Dukhin & Derjaguin, 1974; Pride, 1994; Warden et al., 2013; Zyserman et al., 2017). An alternative is to use the movable (effective) excess charge density $\hat{Q}_{\mathrm{v}}^{*}$ (C/m^{3}) and permeability to directly relate the relative flow to streaming current generation (Revil & Linde, 2006). The cross-coupling coefficient calculated by both approaches explains some experimental measurements (Bordes et al., 2015; Revil & Mahardika, 2013; Zhu & Toksöz, 2013). In terms of partially-saturated conditions considering only water and air in the pore space, the latter approach conveniently relates $L^*(\omega)$ to the effective permeability and $\hat{Q}_\mathrm{v}^*$ as functions of the water saturation by (Revil & Mahardika, 2013; Soldi et al., 2020):

$$L^*(\omega, S_\mathrm{w}) = \frac{k^*(\omega, S_\mathrm{w})\hat{Q}_\mathrm{v}^*(\omega, S_\mathrm{w})}{\eta_\mathrm{w}}. \tag{9}$$

The frequency-dependent (dynamic) characteristics of permeability and effective excess charge density are approximately described by the relaxation time or the angular transition frequency ω_t $(\mathrm{rad/s})$, which determines the transition from the viscous (low frequency) to inertial laminar flow (high frequency) (Revil & Mahardika, 2013). $\omega_\mathrm{t}(S_\mathrm{w})$ is expressed as a function of water saturation by Revil and Mahardika (2013) and Solazzi et al. (2020):

$$\omega_\mathrm{t} = \frac{\eta_\mathrm{w}\phi S_\mathrm{w}}{\rho_\mathrm{w} k_0(S_\mathrm{w})\tau_\mathrm{w}(S_\mathrm{w})}, \tag{10}$$

where τ_w denotes the tortuosity related to the topology of the pore space. The saturation-dependent tortuosity is equivalent to $\phi F {S_\mathrm{w}}^{(1-n)}$ based on Archie's law (e.g., Niu & Zhang, 2019; Jougnot et al., 2018; Revil et al., 2007; Revil & Jougnot, 2008). Since $n \geq 1$ $(1 - n \leq 0)$, the tortuosity increases with the decrease of water saturation (e.g., Ghanbarian et al., 2013; Jougnot et al., 2018), while the transition frequency increases with the decrease of water saturation. Here, $k_0(S_\mathrm{w})$ denotes the quasi-static $(\omega = 0)$ effective permeability as a function of saturation. When the frequency-dependent effective permeability and excess charge density are considered, Equation 9 is written by (Revil & Mahardika, 2013):

$$L^*(\omega, S_\mathrm{w}) = \frac{k_0(S_\mathrm{w})\hat{Q}_{\mathrm{v},0}(S_\mathrm{w})}{\eta_w\sqrt{1 - \frac{i\omega}{\omega_\mathrm{t}}}}. \tag{11}$$

There are two main approaches to describe this effective excess charge density $\hat{Q}_{\mathrm{v},0}$: either by volume-averaging (Linde et al., 2007a) or flux-averaging (Jougnot et al., 2012). In this work, the excess charge density at a saturated state is estimated from permeability using (Jardani et al., 2007):

$$\log10(\hat{Q}_{\mathrm{v},0}^{\mathrm{sat}}) = -0.82\log10(k_0^{\mathrm{sat}}) - 9.23. \tag{12}$$

The superscript ‘sat’ denotes a fully saturated condition. This empirical relationship has been applied to various samples ranging from different salinities and lithologies even if it did not consider the effect of salinities of pore water on the excess charge density (Jardani et al., 2007; Jougnot et al., 2015).

Another empirical relationship between the voltage coupling coefficient under saturated conditions C_0^{sat} (mV/m) and the electrical conductivity of pore water σ_{w} (S/m) is expressed as (Linde et al., 2007b):

$$\log(|C_0^{\mathrm{sat}}|) = -0.895 - 1.319\log(\sigma_{\mathrm{w}}) - 0.1227[\log(\sigma_{\mathrm{w}})]^2, \tag{13}$$

where σ_{w} is estimated by the salinity C_{w} (mol/L) (Sen & Goode, 1992):

$$\sigma_{\mathrm{w}} = (5.6 + 0.27T - 1.5 \times 10^{-4}T^2)C_{\mathrm{w}} - \frac{(2.36+0.099T)C_{\mathrm{w}}^{\frac{3}{2}}}{1+0.214C_{\mathrm{w}}}, \tag{14}$$

where T is the temperature in Celsius (°C). Thus, the voltage coupling coefficient C_0^{sat} varies with pore water salinity. Compared with laboratory and field measurements, Equation 13 works well in a range of 10^{-2} – $10^{0.5}$S/m for σ_{w}, which covers typical pore water environments (Linde et al., 2007b, Jougnot et al., 2015; Hu et al., 2020). By changing the unit of C_0^{sat} to V/m, it can be transformed from the static coupling coefficient L_0^{sat} (A/m^2) by:

$$C_0^{\mathrm{sat}} = -\frac{L_0^{\mathrm{sat}}}{\sigma_0}. \tag{15}$$

Further, C_0^{sat} can be used to express the $\hat{Q}_{\mathrm{v},0}^{\mathrm{sat}}$ with:

$$\hat{Q}_{\mathrm{v},0}^{\mathrm{sat}} = -\frac{C_0^{\mathrm{sat}}\sigma_0\eta_w}{k_0^{\mathrm{sat}}}. \tag{16}$$

We may use Equation 12 to estimate $\hat{Q}_{\mathrm{v},0}^{\mathrm{sat}}$ under a known k_0^{sat}or we may derive $\hat{Q}_{\mathrm{v},0}^{\mathrm{sat}}$ by Equations 13-16 using the salinity of pore water (Jougnot et al., 2015). Otherwise, C_0^{sat} can be obtained by measuring the voltage differences and hydraulic pressure differences of samples to calculate values of $\hat{Q}_{\mathrm{v},0}^{\mathrm{sat}}$ by Equation 16.

For partially saturated conditions, we applied the volume-averaging method to scale $\hat{Q}_{\mathrm{v},0}$ by the effective saturation $S_{\mathrm{e}} = \frac{S_{\mathrm{w}} - S_{\mathrm{wr}}}{1 - S_{\mathrm{wr}}}$ (Linde et al., 2007a; Revil & Cerepi, 2004; Revil et al., 2007):

$$\hat{Q}_{\mathrm{v},0}(S_{\mathrm{w}}) = \frac{\hat{Q}_{\mathrm{v},0}^{\mathrm{sat}}}{S_{\mathrm{e}}}, \tag{17}$$

where S_{wr} (unitless) denotes the residual (irreducible) water saturation. Alternative formulations have been derived to explicitly describe the dynamic process of $\hat{Q}_{\mathrm{v},0}$ varying with water saturation based on the characteristic pore-size distribution (Jackson, 2010; Jougnot et al., 2012; Soldi et al., 2020; Solazzi et al., 2022). Furthermore, the frequency-dependent effective excess charge density is calculated by applying a scaling factor $\sqrt{1 - \frac{i\omega}{\omega_t}}$ (Revil & Mahardika, 2013), which also has been further developed by Jougnot and Solazzi (2021) and Thanh et al. (2022).

Apart from the effective permeability and excess charge density, other effective parameters (e.g., the electrical conductivity σ^*, the mass density of fluid ρ_{f}) in Equations 1 and 2 strongly depends on the water saturation as well. Besides, the two fluid phases in the pore space affect the mechanical properties (e.g., the effective bulk moduli) that need to be considered in hydromechanical modeling of the volumetric strain of porous media and the infiltration displacement (Equations 3-5). This indicates that seismic signals could respond to variations in water saturation. We summarize the frequency-dependent (dynamic) and saturation-dependent parameters in Table A3 of Appendix A. More details with regard to the parameters mentioned above as well as the derived equations can be found in Revil & Mahardika (2013).

2.2. Multi-Channel SeismoElectric Spectral Ratios (MC-SESRs)

For isotropic layered media, as the SE field and the seismic particle acceleration field are triggered by the same seismic source, the seismic source function can be canceled when we calculate the ratios of SE fields to the seismic acceleration fields in the frequency domain (Dzieran et al., 2019). Therefore, the SESRs can be represented by the ratio of their Green's functions $GE(\omega)$ and $Ga(\omega)$, which is expressed as (Dzieran et al., 2019):

$$\mathrm{SESR}(\omega) = \frac{\mathbf{E}(\omega)}{\boldsymbol{a}(\omega)} = \frac{GE(\omega)}{Ga(\omega)}, \tag{18}$$

where $\mathbf{E}(\omega)$ denotes the SE field spectra. $\boldsymbol{a}(\omega)$ denotes the seismic ground acceleration field spectra, which also can be replaced by the components of seismic ground velocity spectra with $i\omega\mathbf{v}(\omega)$ or displacement spectra with $-\omega^2\mathbf{u}(\omega)$. The SESR indicates the ratio of Green's functions, which contains the information of stratified porous media. The modulus of SESRs varies with position, or offset from the seismic source, represented by:

$$\text{MC-SESR}(\omega, x_i) = \frac{|E_{x,i}(\omega)|}{|a_{x,i}(\omega)|}, i = 1, 2, \ldots, B \tag{19}$$

where i denotes the measured points and B is the total number of measured points. Here, $E_{x,i}$ and $a_{x,i}$ denotes the horizontal electric field and seismic ground acceleration in the frequency domain at point i.

2.3. Inversion framework

Deterministic inverse modeling (e.g., Gauss-Newton, Conjugate Gradient, Levenberg-Marquardt) algorithms need to construct an objective function, including the data misfit and a regularization term. The latter depends on prior and empirical information. In weakly non-linear problems, the iterative adjustment of model parameters using gradient-based information enables a minimum objective function to be attained. However, it is time-consuming when we deal with high-dimension parameter estimation, and these parameters affect the SESRs in a non-linear way. Furthermore, such deterministic inversions might fail to recover the true model, although the modeling data well match the observed data (Wu et al., 2021).

In this study, we aim to reconstruct the permeability and water table depth using the near-surface MC-SESRs data. As the water table is affected by land-management practices, precipitation, evapotranspiration, and other environmental changes, its depth may change with time. Machine learning techniques may allow us to efficiently monitor the dynamic water table. A large number of samples are employed to train a neural network, which can construct the mapping process between the input data (MC-SESRs) and the output data (water table depth and permeability). Once the neural network is well trained, we can adapt it to a specific region to monitor variations of its water table and permeability efficiently. Deep-structured neural networks have been employed in solving geophysical inverse problems (e.g., Laloy et al., 2021; Wu et al., 2021), which are alternatives for the SESRs inversion. But the many hidden layers included in such networks produce a large quantity of hyperparameters, which need large data sets and many training epochs to be estimated. Complicated deep architectures empower the neural network to project a more complex relationship between the input and output layers. However, the computing time is increased due to the iterations of training epochs, and overtrained networks could result. Chen and Liu (2017) propose a broad learning (BL) neural network that adopts a flat architecture without a complex multilayer structure. Its network structure does not change within the training process (Figure 2). It avoids adjusting elusive hyperparameters in the network, and its design largely decreases the training time compared with deep networks. Broadly expanding the mapping layer enhances the capacity of the neural network to approach complicated projecting relationships. More important, the broadly expanding structure can be used for incremental learning without retraining the network when additional data are available in input data (Chen & Liu, 2017). Compared with the performance of deep structured neural networks (e.g., deep convolutional neural networks, deep Boltzmann machines, and deep belief networks) on MNIST and NORB data sets, Chen and Liu (2017) demonstrated that the BL system can ensure a comparable classification accuracy while vastly reducing the training time. Recently, the BL approach has been applied to effectively and efficiently process classification and regression problems (Gong et al., 2022). Therefore, the BL approach is considered here to perform water table depth and permeability inversions using MC-SESRs data.

As a supervised machine learning task, we need to generate a large number of training samples. We assume the number of samples is N for training the network and the number of inverted layers of permeability is L. If there are A frequencies and B measured points (traces) in Equation 19, the input matrix $\mathbf{X}$ is MC-SESRs data (Figure 2a). The output matrix $\mathbf{Y}$ is made up of N depths of the water table written by a vector $\mathbf{dwt}_{N\times 1}$ and $N \times L$ permeability matrix written by $\mathbf{K}_{N\times L}$ (Figure 2c). Using the neural-network architecture of the BL model (Chen & Liu, 2017), we first need to extract the features of MC-SESRs data as the input layer (Figure 2b):

$$\mathbf{F}_i = \varphi_i(\mathbf{X}\mathbf{W}_i + \boldsymbol{\beta}_i), i = 1, 2, \ldots, Q \tag{20}$$

where $\mathbf{F}_i$ denotes the ith mapped feature matrix. $\mathbf{W}_i$ and $\boldsymbol{\beta}_i$ denote the random weighting matrix and bias term, which are initially generated by standard uniform distributions in a range of [-1,1]. Assuming $A \times B = C$, the sizes of matrices of $\mathbf{W}_i$ and $\boldsymbol{\beta}_i$ are $C \times P$ and $N \times P$, respectively. As shown in Figure 2b, P is the number of feature nodes in each mapping feature group i. Q is the number of mapping features. The function φ_i maps the sum of matrices $\mathbf{X}\mathbf{W}_i + \boldsymbol{\beta}_i$ to [-1,1] by normalizing the minimum and maximum value each row (1,2, …, N). The sparse autoencoder is employed to shrink the input data and extract its mapping features by adapting $\mathbf{W}_i$ (Chen & Liu, 2017). As shown in Equation 20, this feature extracting step of the input data can be replaced by other extracting approaches from popular artificial neural networks (e.g., deep convolutional neural networks) (Gong et al., 2022).

The features of input data extracted by mapping feature groups $\mathbf{F}^Q = [\mathbf{F}_1, \mathbf{F}_2, \ldots, \mathbf{F}_Q]$ are broadly expanded by M enhancement nodes with:

$$\mathbf{E}_j = \xi_j([\mathbf{F}_1, \mathbf{F}_2, \ldots, \mathbf{F}_Q]\mathbf{W}_{ej} + \boldsymbol{\beta}_{ej}), j = 1, 2, \ldots, M \tag{21}$$

where $\mathbf{E}_j$ denotes the matrix of jth enhancement node. $\mathbf{W}_{ej}$ and $\boldsymbol{\beta}_{ej}$ are randomly generated similar to Equation 20. In this study, we used the hyperbolic tangent sigmoid transfer function as the non-linear activation function $\xi_j(\cdot)$. Each enhancement node is integrated to an enhancement layer with $\mathbf{E}^M = [\mathbf{E}_1, \mathbf{E}_2, \ldots, \mathbf{E}_M]$.

The output-layer hydrogeological parameters $\mathbf{Y} = [\mathbf{dwt}, \mathbf{K}]$ and the last layer integrated by input features and the enhancement layer are connected by a weighting matrix $\mathbf{W}^M$:

$$\mathbf{Y} = \left[\mathbf{F}_1, \mathbf{F}_2, \ldots, \mathbf{F}_Q \middle| \mathbf{E}_1, \mathbf{E}_2, \ldots, \mathbf{E}_M\right]\mathbf{W}^M, \tag{22}$$

Therefore, the training process only needs to estimate the connected-link matrix $\mathbf{W}^M$ through solving the pseudoinverse matrix $[\mathbf{F}^Q|\mathbf{E}^M]^+$:

$$\mathbf{W}^M = [\mathbf{F}^Q|\mathbf{E}^M]^+\mathbf{Y}. \tag{23}$$

Following Chen and Liu (2017), the ridge regression approximation is employed to optimize $\mathbf{W}^M$ by fulfilling:

$$\arg\min: \|[\mathbf{F}^Q|\mathbf{E}^M]\mathbf{W}^M - \mathbf{Y}\|_2^2 + \lambda\|\mathbf{W}^M\|_2^2, \tag{24}$$

where λ denotes a tradeoff regularization factor and $\|[\mathbf{F}^Q|\mathbf{E}^M]\mathbf{W}^M - \mathbf{Y}\|_2^2$ is the error term of the training set. Except for the connected matrix $\mathbf{W}^M$, the remaining weight matrices in the network are randomly generated. Consequently, we can use the well-trained network with the optimal connected weights $\mathbf{W}^M$ to invert MC-SESRs data. For example, if we acquired more MC-SESRs data, we just need to replace Input $\mathbf{X}$ with the new (untrained) data in Equation 20. By following similar computations to the training process by Equations 20-22, we then extract the mapping features of the inversion data and use an activation function to learn these features in the enhancement layer. Thus, we obtain the newly mapped feature matrices and enhancement matrices. Multiplied with the weight matrix derived from the training process (Equations 23 and 24), we can obtain the estimated water table depth and permeability (Equation 22).

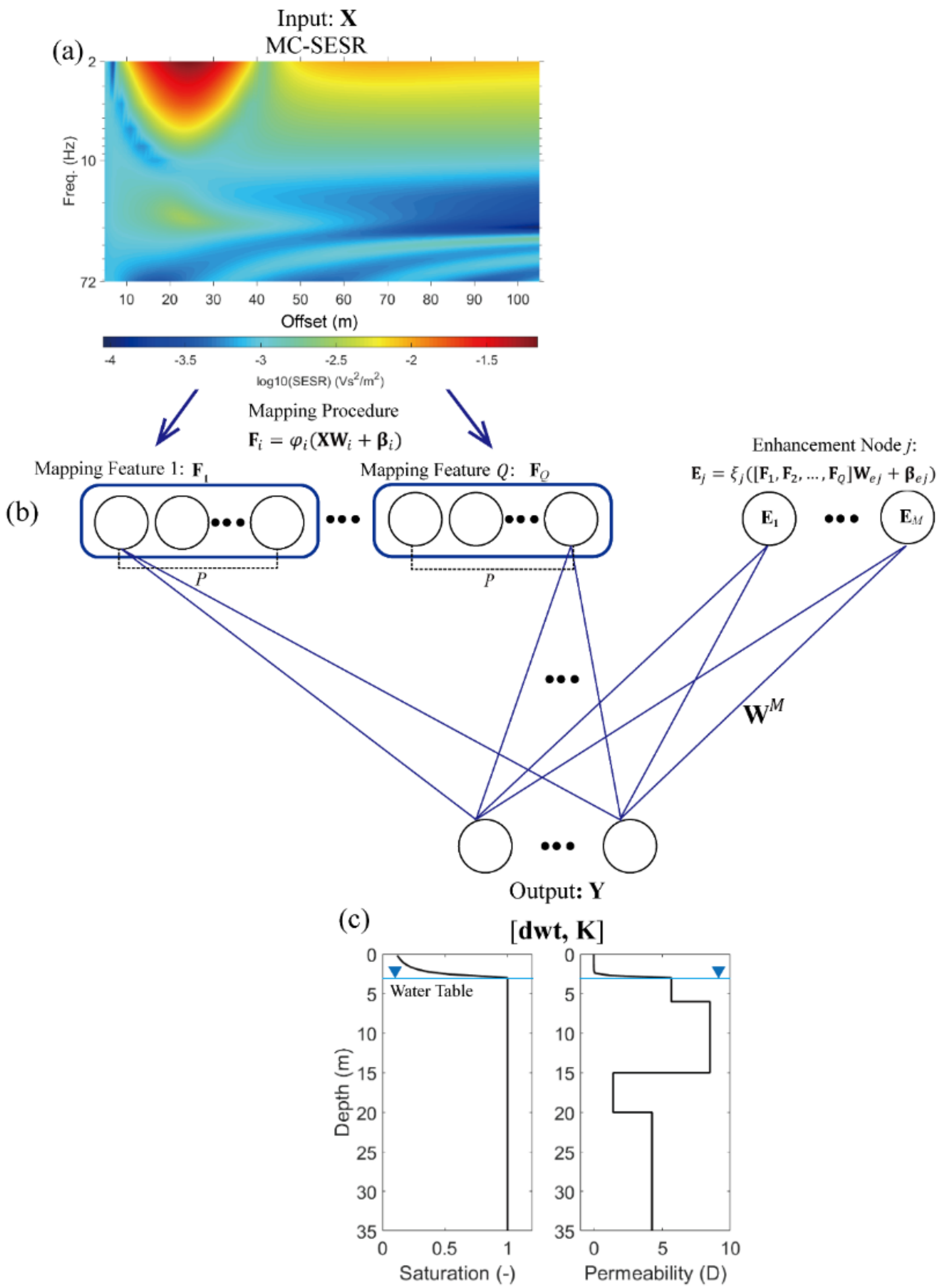

Figure 2. Broad learning (BL) procedure including (a) the input (MC-SESRs data) layer, (b) the mapping feature layer and the enhancement layer, and (c) the output (permeability with water table) layer employed in this study.

3. Sensitivity Analysis

3.1. Basic test model

We first design a basic test model (Figure 3). It consists of five horizontal layers of porous materials. It is assumed that the shallow two layers (layers 1-2) are mainly made up of loamy sands, and the deeper two-layer soils (layers 3-4) with lower permeabilities considered as silty sands. The bottom layer 5 is assumed as a known layer with lower permeability (0.01 D), porosity (0.05), and electrical conductivity (16 $\mu\mathrm{S/cm}$). These hydrogeological parameters are chosen based on Carsel and Parrish (1988). The initial water table is set at 3 m, implying that the shallowest layer is partially saturated (Figure 3a). The Richards' equation (Richards, 1931) is used to solve the hydraulic problem in the vadose zone. The Mualem-van Genuchten (MVG) empirical model (Mualem, 1976; van Genuchten, 1980) is used to estimate the relationship between the water saturation and the effective permeability with the pore pressure. Based on the MVG model by introducing the soil-water characteristic parameters α_{VG} (m^{-1}), n_{VG} and $m_{\mathrm{VG}} = 1 - 1/n_{\mathrm{VG}}$, the effective water saturation S_{e} and the static permeability k_0 at partially saturated conditions are expressed by:

$$S_{\mathrm{e}} = \frac{1}{\left[1+(\alpha_{VG}|H_{\mathrm{p}}|)^{n_{\mathrm{VG}}}\right]^{m_{\mathrm{VG}}}}, \tag{25}$$

$$k_0 = k_0^{\mathrm{sat}} S_{\mathrm{e}}^{\frac{1}{2}} \left[1 - \left(1 - S_{\mathrm{e}}^{\frac{1}{m_{\mathrm{VG}}}}\right)^{m_{\mathrm{VG}}}\right]^2. \tag{26}$$

Here, we assume that the absolute pressure head $|H_{\mathrm{p}}|$ (m) in the vadose zone is equal to the vertical distance between its elevation and the position of the water table (Zyserman et al., 2017). The effective electrical conductivity is calculated by Equation 7, whose formulas and the used parameters are given in Table A3 of Appendix A and Table S1 of the Supporting Information). The water saturation, the effective permeability, and the effective electrical conductivity of the top four layers are presented in Figures 3b-d under the assumption that the pore water salinity is homogeneous at 2×10^{-3} mol/L at 293.15 K, respectively. Note that the effect of the salinity at this level on the fluid mass density is negligible. In contrast, the mass density of the fluid solute should be considered in a highly saline environment (e.g., Hu et al., 2023). The specific parameters of each layered material are given in Table 1, whose descriptions can be found in Table A2 of Appendix A.

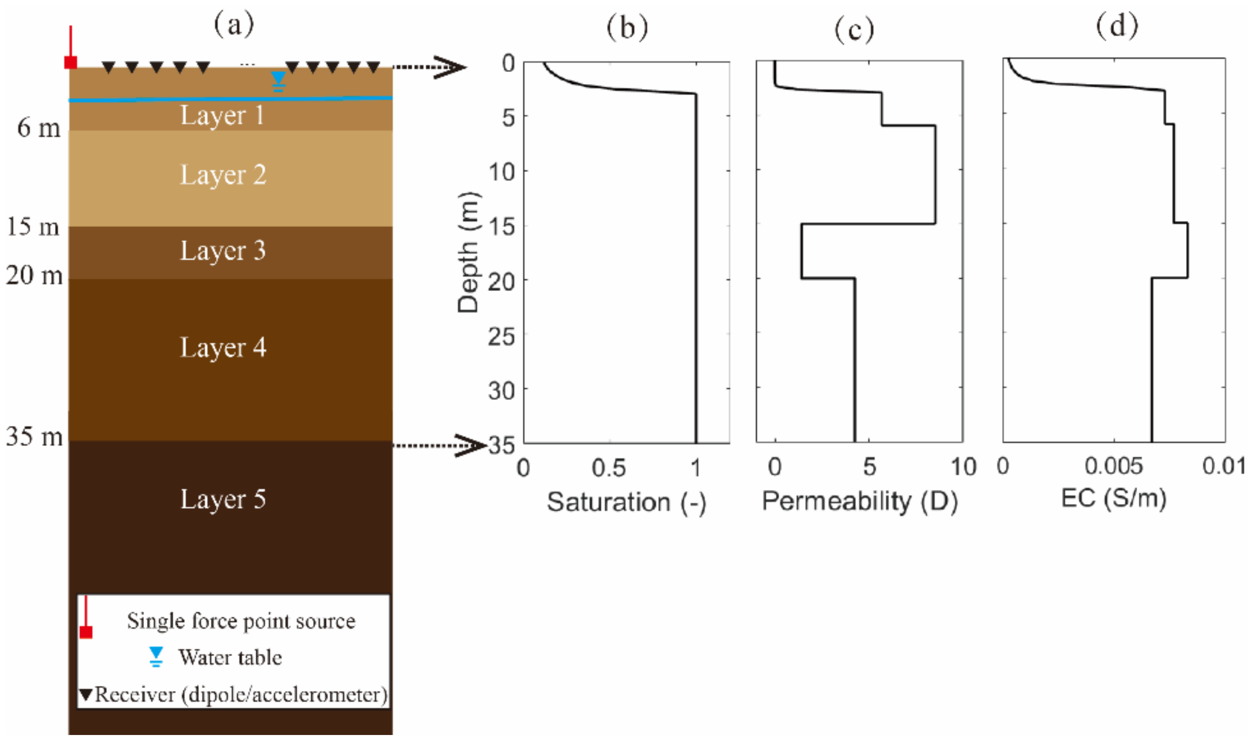

Figure 3. Basic test model and its observations. (a) Geometry, (b) water saturation, (c) effective permeability, and (d) effective electrical conductivity in the top four layers

There is a vertical force point source at the ground marked with a red square in Figure 3a. We assume that the seismic source function $f_s(t)$ (N) presents as a Ricker wavelet with a peak frequency f_p of 20 Hz:

$$f_s(t) = -2.506 \times 10^5 \left[1 - 2(\pi f_p)^2 \left(t - \frac{2}{f_p}\right)^2\right] \exp[-(\pi f_p)^2 (t - \frac{2}{f_p})^2]. \quad (27)$$

The spectrum of this zero-phase wavelet is in a range of ~ 70 Hz. This wavelet and its frequency band are usually considered in seismoelectric simulations (e.g., Jardani et al., 2010). Equation 27 is applied to calculate the body force of Equation 5 in forward modeling. Receivers are installed at 0.1 m below the ground surface. The offset ranges from 5 – 105 m with 101 horizontal acceleration sensors and 101 horizontal point dipoles. The offset represents the distance between the source and each accelerometer or central point of each dipole. The interval of two adjacent receivers is 1 m (Figure 3a). Please note that the seismic particle velocity $\mathbf{v}(\omega)$ obtained by geophones could also be used to calculate SESRs by transforming $\mathbf{a}(\omega)$ to $i\omega\mathbf{v}(\omega)$. As mentioned in Section 2.2, measuring SESRs does not require knowledge of the seismic source function, so we would not need to know the amplitude of the seismic source. Additionally, the SE responses are proportional to the amplitude of seismic sources, either for explosive sources or weight drops, demonstrated in the field tests (Butler et al., 1999). Therefore, according to the specific prospecting conditions, this seismic source function can be replaced with other source functions. However, the seismic strength and waveform used here are adopted to illustrate that the predicted electric fields are expected to be measurable for a reasonable seismic source.

Based on Section 2.1, with the dynamic and saturation-dependent parameters chosen, especially the cross-coupling coefficient $L^{*}(\omega, S_{\mathrm{w}})$ in Equation 11, the peak-trough averaging approach based on Luco-Apsel-Chen Generalized Reflection and Transmission Method (LAC GRTM) (Zheng et al., 2021) is applied to obtain the frequency solution of the governing equations. The wave-field components are derived from the numerical integral over the wavenumber domain. The integrand includes the Bessel function and exponential terms of fast and slow *P*, *S*, and EM waves. Compared with the seismic wavelength, the relatively small source-receiver vertical differences make integrands more intensively oscillate. Therefore, this situation may cause a slow convergence computationally (Zheng et al., 2021). The peak-trough averaging approach uses a certain wavenumber interval in a stably oscillating range to determine peaks and troughs of integrands and subsequently apply the repeat average method to efficiently compute the numerical integration (Dahlquist & Björck, 1974). Thus, it allows us to consider more flexible source-receiver geometries. All used dynamic and saturation-dependent parameters and corresponding formulations are given in Table A3 of Appendix A, and we summarize a flow chart of the model generation in Figure 4. We assume that the data recorded from 0 to 0.5 s is digitized by 4096 samples with a sample interval of 0.1221 ms. After the full-waveform computation of this model, we display the horizontal components of seismic ground acceleration and SE wave fields (Figure 5). Since a zero-phase wavelet was applied to simulate the seismic source (Equation 27), a time delay is shown in the waveforms (Figure 5). In addition, due to a low saturation ($S_{\mathrm{w}} = 0.12$) occurring on the near-surface (~0.3 m), the corresponding *S*-wave velocity is 1242.5 m/s. The surface waves can have a high apparent velocity to present in longer source-receiver offsets than the offset range shown in Figure 5. In this case, the maximum absolute horizontal electric field is 26.27 μV/m. Although the electric-field signals are vulnerable to noise, the environmental noise level can be managed to below the order of 0.1 μV/m (see Butler et al., 2007; Dupuis et al., 2007;

Thompson & Gist, 1993). The near-surface electric field of this case is, hence, sufficient to be observed.

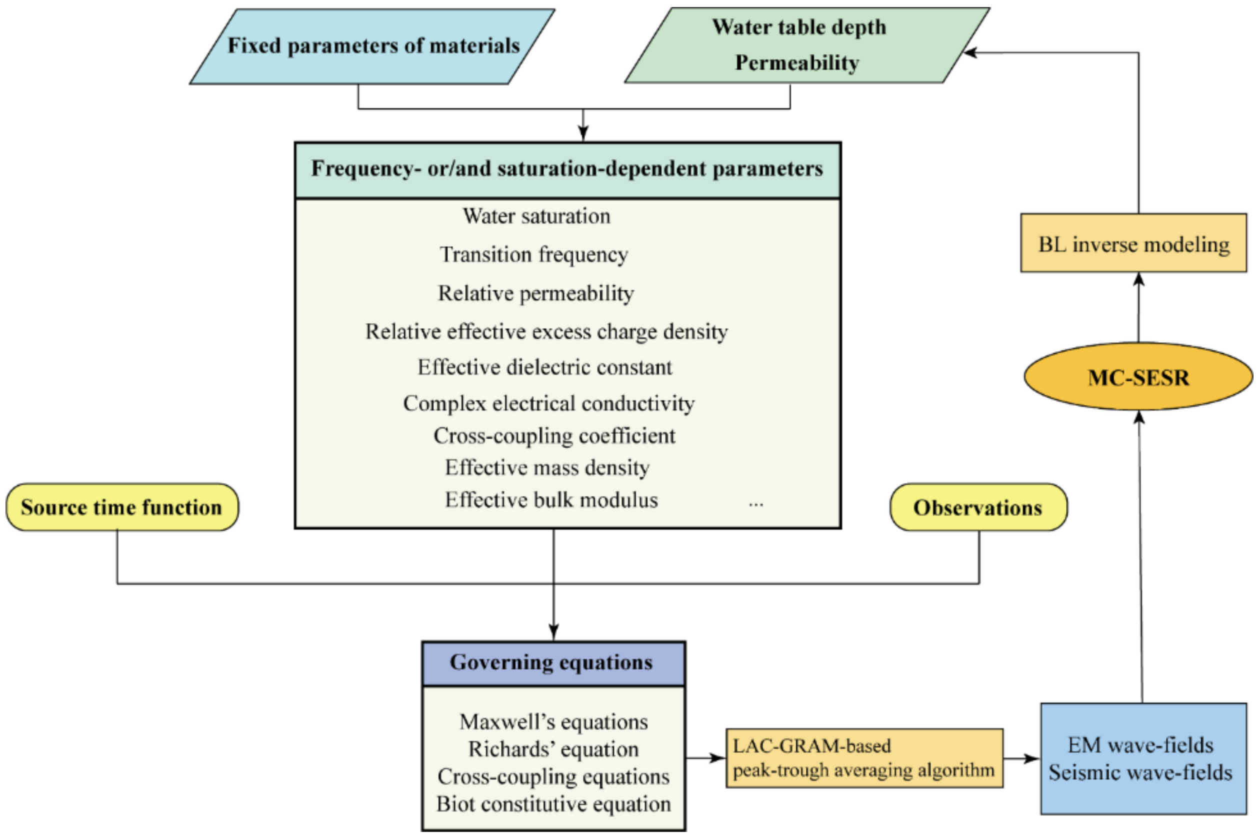

Figure 4. Framework of MC-SESRs generation

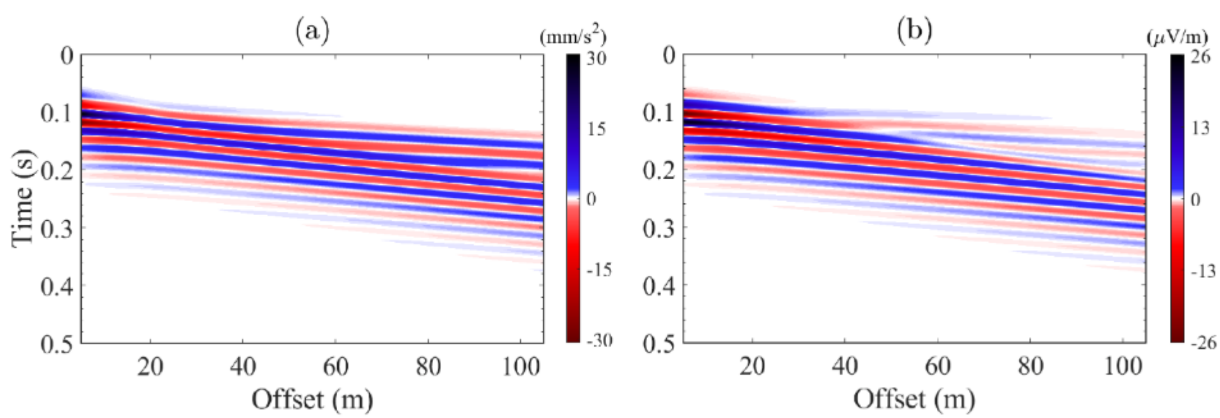

Figure 5. Horizontal components of wave fields under the basic test model (a) seismic ground acceleration and (b) seismoelectric wave fields

The horizontal components of seismic ground acceleration and SE wave fields recorded in the time domain are subsequently transformed into the frequency domain. Then the MC-SESRs over the full 0.5s time window are calculated by Equation 19. Here, we take the frequency in the range of 2-72 Hz. The MC-SESRs' contour map of this numerical model is shown in Figure 6a. The SESRs with greater strength are mainly distributed in a short-offset range (10 - 40 m) and a low-frequency range (~ 10 Hz). Since the SESR concept under the assumption of the localized (coseismic) SE field waves are linear with the ground acceleration, the frequency-dependent behaviors depend on the evanescent and radiated SE field waves (Dizeran et al., 2019). The generation of the radiated SE field waves is commonly regarded as caused by the seismic waves nearly vertically arriving at interfaces and the ground surface. Although the radiated EM waves generated by the direct SE conversions at the source also depend on the frequency, their strength is weak. The subsurface properties' variations barely affect the component of MC-SESRs originating from the direct SE conversions.

Once the seismic incident angle is larger than the critical angle θ_c:

$$\theta_\mathrm{c} = \arcsin\left(\frac{V_\mathrm{sei}}{V_\mathrm{EM}}\right), \tag{28}$$

where V_sei (m/s) and V_EM (m/s) denote the seismic wave velocity and EM wave velocity, respectively, the SE conversion leads to the generation of evanescent SE waves. Actually, θ_c approaches zero due to $V_\mathrm{EM} \gg V_\mathrm{sei}$. The existence of physical properties' contrasts causes the interfacial SE responses, mainly containing evanescent SE field waves. The superposition of different modes of SE conversions makes the spectral ratios between the SE responses and the ground acceleration are of frequency dependence. Thus, the SESR modulus decreasing with the increasing frequency mainly attributes to the evanescent SE waves, which approximately decay with a factor $\exp(-\omega p \Delta z)$ (Ren et al., 2018). The horizontal EM wave slowness p relies on the incident angle of the seismic waves arriving at the interface and inducing the localized SE waves. The spatial variations of SESRs presumably are complicated due to the presence of a vadose zone. The multi-channel SE field waves combined with the ground acceleration field waves are sensitive to water table variations (e.g., Rabbel et al., 2020). Using MC-SESRs facilitates the inversion of hydrogeological parameters due to without reconstructing the seismic source function. Selecting SESRs from near- and far-offset receivers, we show the SESRs varying over frequency for three receivers with different offsets of 5 m, 30 m, and 50 m, respectively. As shown in Figures 6b-d, the SESRs at different offsets have a similar frequency dependence. The SESR generally increases as the frequency decreases, and their log-scale variations show an approximately linear correlation in the low-frequency domain (~10 Hz), and it oscillates at higher frequencies. Notably, the oscillating signatures are more notable in the far-offset range (Figures 6c-d). These oscillatory characteristics may originate from the electric field induced by the guided *P*-wave traveling in the upper two layers.

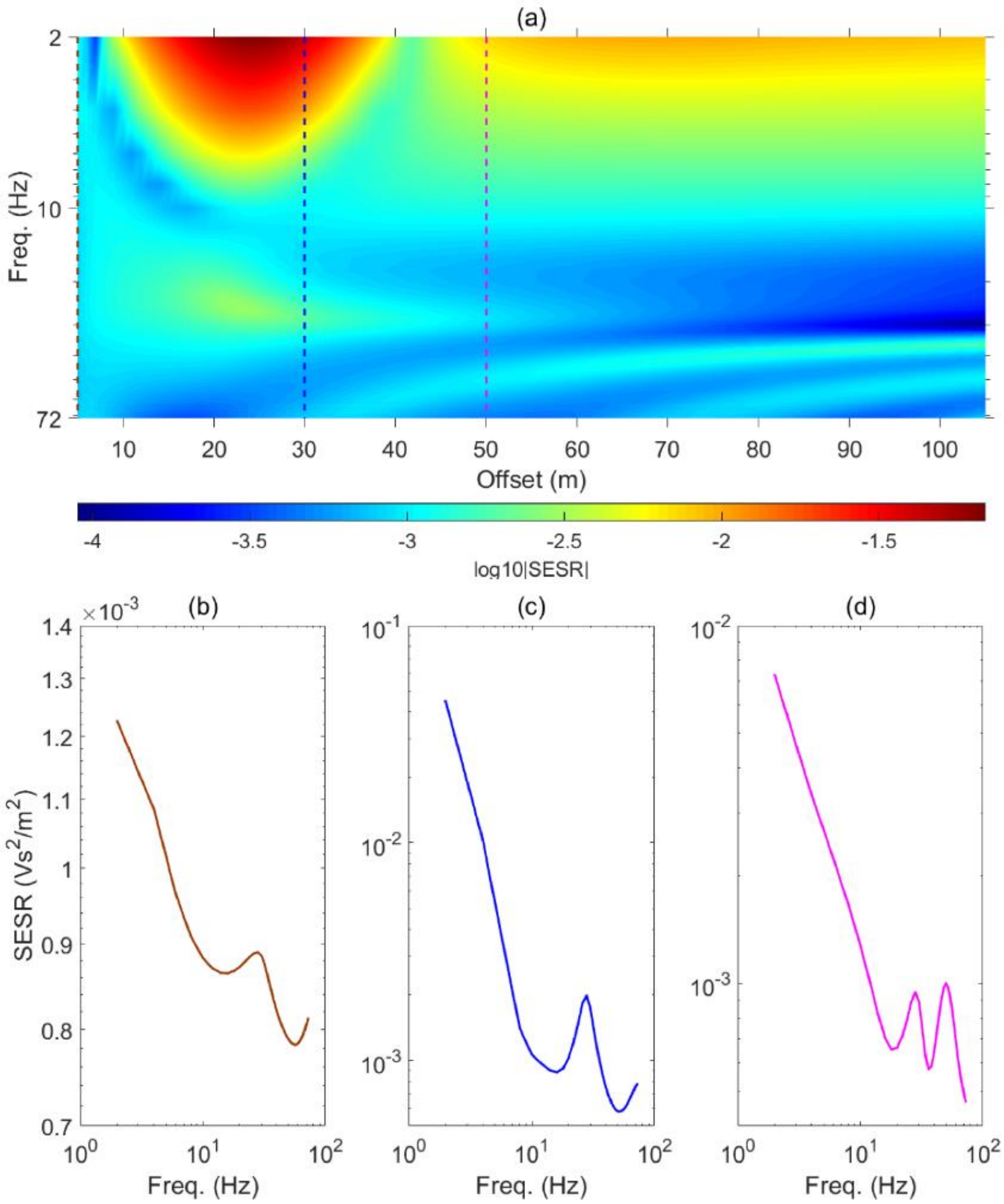

Figure 6. The MC-SESRs of the basic test model with (a) the contour map of MC-SESRs in logarithmic scale showing variations both with frequency and offsets. Sample SESR curves as a function of frequency at different offsets: (b) 5 m, (c) 30 m and (d) 50 m.

Table 1

Parameters of the basic test model

Property	Units	Layer 1	Layer 2	Layer 3	Layer 4	Layer 5
Thickness	m	6	9	5	15	Inf.
ϕ	$\mathrm{m^3/m^3}$	0.41	0.43	0.46	0.38	0.05
α_{VG}	$\mathrm{m^{-1}}$	12.4	-	-	-	-
n_{VG}	-	1.89	-	-	-	-
S_{wr}	-	0.1585	-	-	-	-
ρ_{s}	$\mathrm{kg/m^3}$	2650	2650	2650	2650	2700
ρ_{w}	$\mathrm{kg/m^3}$	1000				
ρ_{a}	$\mathrm{kg/m^3}$	1.21	-	-	-	-
$\rho_{\mathrm{b}}^{\mathrm{sat}}$	$\mathrm{kg/m^3}$	1973.5	1940.5	1891	2023	2615
C_{w}	mol/L	2×10^{-3}				
σ_0^{sat}	S/m	0.0073	0.0077	0.0083	0.0067	0.0016
η_{w}	Pa·s	1×10^{-3}				
η_{a}	Pa·s	1.8×10^{-5}	-	-	-	-
T	K	293.15				

κ_s	-	4				
κ_w	-	80.1				
κ_a	-	1				
m	-	1.35				
n	-	1.85				
K_s	GPa	35	35	35	35	36
G	GPa	2.49	2.49	14.08	14.08	15
K_{fr}	GPa	2.84	2.84	14.4	14.4	20
K_w	GPa	2.25				
K_a	Pa	1.43×10^5	-	-	-	-

554

3.2. Analysis of permeability

First, we test the sensitivity of SESRs with respect to permeability. The considered typical ranges in the critical zone refer to Carsel and Parrish (1988). The saturated permeability k_j^{sat} of the top four layers ($j = 1,2,3,4$) in the basic test model is 5.67, 8.51, 1.42, and 4.26 D, respectively (Figure 3c). By changing the saturated permeability of shallow layers ($j = 1,2,3,4$) $\pm 50\%$, we calculated the absolute MC-SESRs difference concerning the original model by:

$$\Delta\mathrm{SESR}(\omega, x_i, j) = \left|\mathrm{SESR}(\omega, x_i)^{k_j{}^{\mathrm{sat}}+50\%} - \mathrm{SESR}(\omega, x_i)^{k_j{}^{\mathrm{sat}}-50\%}\right|, \tag{29}$$

where the horizontal offset x_i ranges from 5 to 105 m with the number of receivers $i = 1,2,\ldots,101$. The short-offset (~20 m) SESRs have more changes when the permeability of shallow layers has been changed than the permeability of deep layers has been changed (Figure 7). Their maximum absolute differences with changing the saturated permeability of each layer decrease in depth, which is 0.0877, 0.0636, 0.0377, and 0.0069 (Figures 7c, 7e, 7h, and 7l), respectively. The MC-SESRs mainly change in near-offset traces (x_i<45 m) and low frequencies (f< 10 Hz). The absolute differences of SESRs are less when the permeability in the lower zone changes (Figure 7l), whose maximum absolute difference of SESRs is an order of magnitude smaller than for layers 1 and 2. As shown in Figure 7, by changing the permeability of different layers, the absolute differences of SESRs produce different variations either in frequency or laterally.

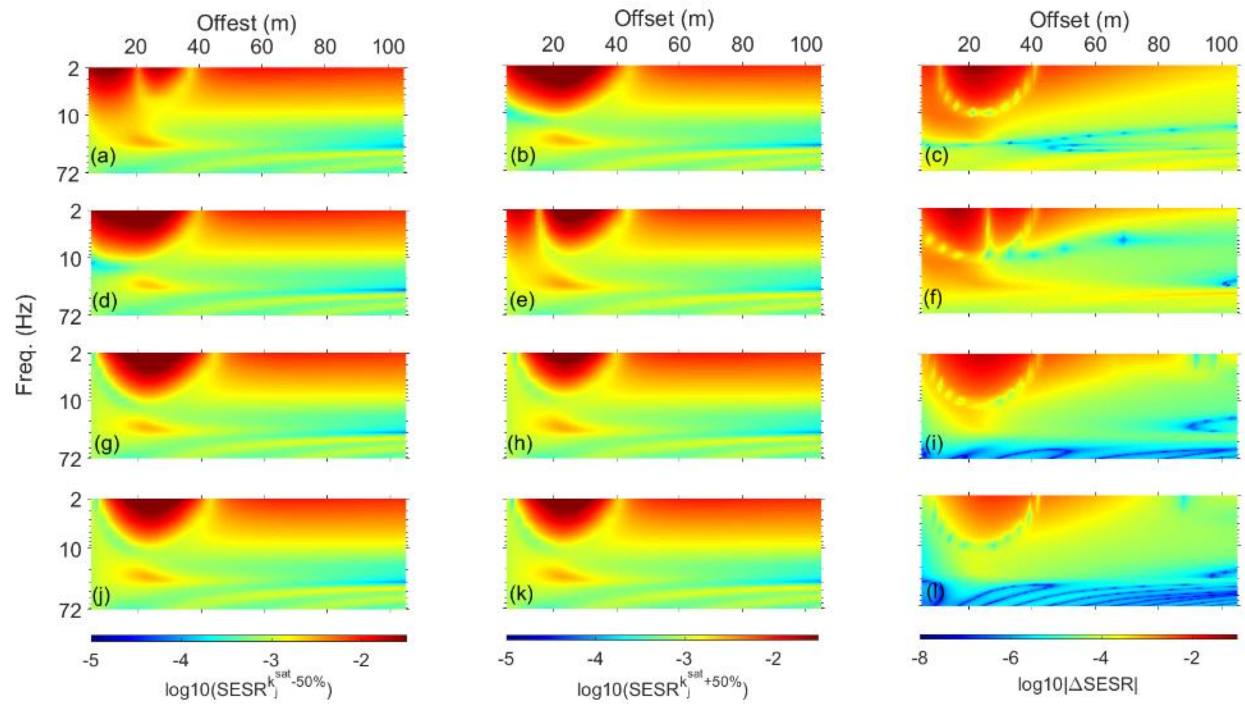

Figure 7. The MC-SESRs in logarithmic scale with respect to (a-d-g-j) 50% decrease and (b-e-h-k) 50% increase the basic test model of (a-c) layer 1, (d-f) layer 2, (g-i) layer 3, and (j-l) layer 4. (c-f-i-l) The absolute MC-SESRs difference in logarithmic scale of the corresponding layers calculated by Equation 29.

To test the behaviors of SE wave-fields by changing the permeability of each layer, we compare the differences between the original waveforms with the changed waveforms in Figure 8. As shown in Figures 8e-h, the variations of SE wave fields are largest when the permeability of layer 2 changes (Figures 8b and 8f). Layer 2 is saturated and provided with the highest saturated permeability in the basic test model. Interestingly, the differences by changing the permeability of layer 1 (Figure 8e) show a very different trend within 0.06 – 0.14 s in contrast with other layers (Figures 8f-h). Layer 1 is a partially saturated zone, which produces a different behavior on waveforms compared with other layers.

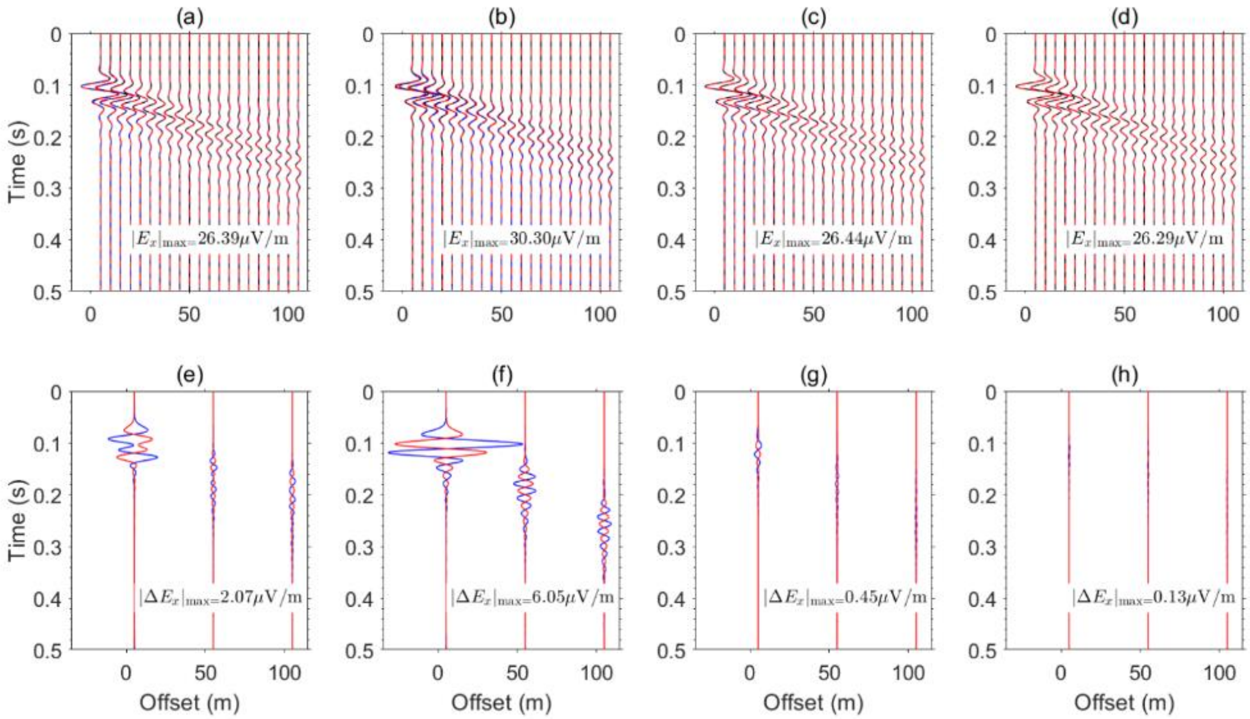

Figure 8. (a-d) Horizontal components of SE wave fields for the basic test model (black solid lines) and for cases of 50% increase (red lines) and decrease (blue lines) in the permeability of layers 1-4 respectively. (e-h) Differences between SE wave fields obtained for cased of 50% increased (red lines)/decreased (blues lines) permeability in layers 1-4 respectively compared to those obtained for the original model, at three particular offsets, whose amplitudes are amplified by a factor of 8 compared to those in (a-d).

3.3. Analysis of water table

Second, we test how the different depths of the water table or partially-saturated conditions influence the distributions of MC-SESRs. Accounting for a static partially-saturated state, the VG model is used to determine the water saturation (van Genuchten, 1980). The water table of the basic test model is assumed to vary seasonally in a year. In this case, we assume the rainy season is from September to November with higher water levels, and the period of March to May is the dry season with lower water levels (Figure 9a). Correspondingly, the water saturation and the effective permeability at the shallow layer change with the water table (Figures 9b-c). As the used parameter α_{VG} ($12.4\ \mathrm{m}^{-1}$) of the VG model is large, the permeability is rather low at low saturations. Note that the contour map of permeabilities shown in Figure 9c is an interpolation result in the time and space domain. Permeabilities below the water level in each layer are different constants, as the basic test model presented in Figure 2c. The SESRs with the short (5 m), medium (30 m), and long (50 m) source-receiver offset are collected to show their responses to the variations of the water table (Figures 9d-f). The absolute ratios increase in the rainy season with higher water levels and decrease in the dry season with lower water levels.

Furthermore, the strength of SESRs in the high-frequency domain is increased when the water table is in the shallow zone (e.g., September-November). The amplitudes of evanescent SE signals decay exponentially with the normal direction of the interfaces (Ren et al., 2016b; Ren et al., 2018). This implies that deep water tables cause weaker SE signals than shallow water tables. This characteristic is also embodied in the SESRs data obtained at the source-receiver offset of 30 m (Figure 9e). Nevertheless, the sensitivity of the SESRs obtained at a more extended offset (50 m) responding to the dynamic water table depth is considerably weakened (Figure 9f). This test implies we may use the time-lapse MC-SESRs data in short source-receiver traces to monitor the water table depth variations.

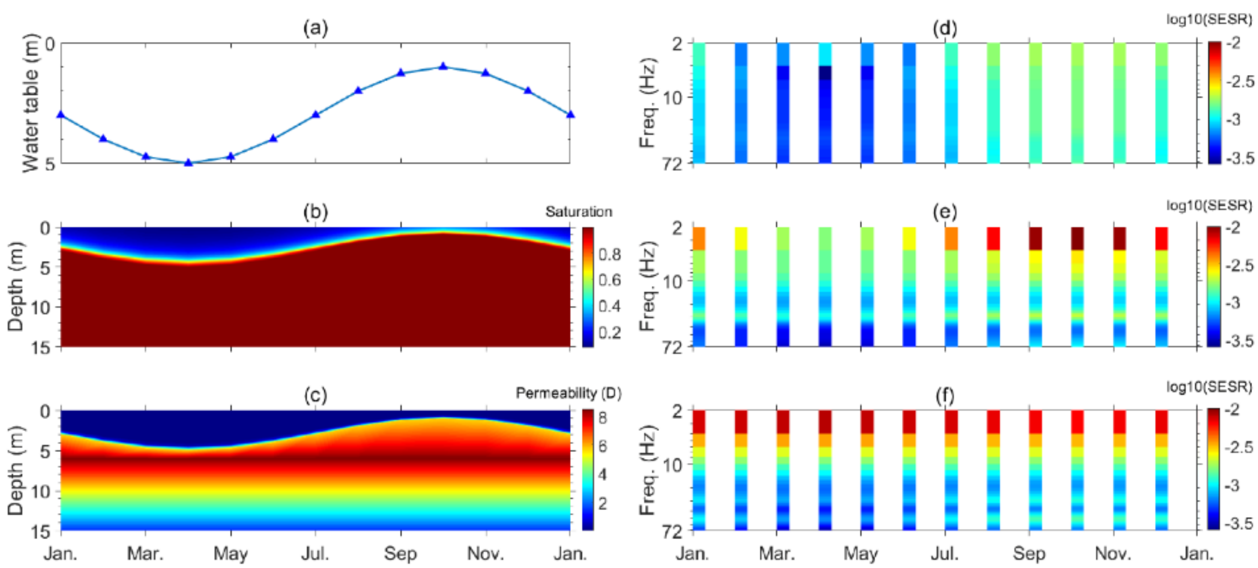

Figure 9. The modeling results with the water table vary over time. (a) The depth of the water table, (b) the time-lapse variations of the water saturation with depth, (c) the effective permeability, and the SESRs in logarithmic scale collected at a source-receiver distance of (d) 5 m, (e) 30 m and (f) 50 m.

4. Inversion Results

Employing synthetic seismic and SE data generated for the basic test model introduced in Section 3.1, we carry out a three-step strategy to perform MC-SESRs inversion. We assume that the depth and properties of the bottom layer 5, and all other layer depths and properties except for the water table depth and the permeabilities of layers 1-4 are known. The prior information could have been determined by drilling and other geophysical methods (e.g., Dzieran et al, 2019). This could represent a scenario where there was interest to monitor temporal changes in depth to the water table and to determine permeabilities of the near surface layers (to 35 m depth) for hydrogeological applications.

To begin, we generated random samples by drawing permeabilities for each of layers 1 - 4 from predefined reasonable ranges, and drawing a water table depth in layer 1 randomly from the range of 1 - 5 m. We account for the ranges of hydraulic conductivity ${K_j}^{\mathrm{sat}}$ of layers 1-2, referring to materials consisting of loamy sands. Layers 3-4 with a lower range of the soil permeabilities are considered to contain more silty sands (Carsel & Parrish, 1988). The hydraulic conductivity of layers 1-2 ranges from 3 to 35 cm/h and layers 3-4 ranges from 0.02 to 15 cm/h, which can be transformed to the ranges of permeability ${k_j}^{\mathrm{sat}}$ by is equal to $\frac{{K_j}^{\mathrm{sat}}\eta_{\mathrm{w}}}{\rho_{\mathrm{w}}\mathrm{g}}$, where g (m/s^2) denotes the gravitational acceleration (9.81 m/s^2). Following the flowchart of the model generation (Figure 4), we calculated MC-SESRS of 7000 random samples. Therefore, the first step is to obtain the 7000 input-output pairs.

4.1. Performance of the BL neural network

In the second step, we randomly selected 5000 from the 7000 input-output pairs for training the BL neural network (Figure 2). In addition, 1500 randomly generated samples were split into the original validation dataset (500 samples) and the original testing dataset (1000 samples). The input MC-SESRs data of the training samples are noise-free synthetic data, and output data are the dwt and the permeability of layers 1-4 (k1, k2, k3, k4) (Figure 2c). First, to accurately extract and map features of the input data, we need to set the number of mapping groups (Q) and feature nodes (P) of each group and their corresponding enhancement nodes (M) based on the BL architecture (Figure 2) introduced in Section 2.3. After that, the BL network is fixed. We tested different configurations of the BL neural network to present the root-mean-squared errors (RMSEs) of training models (water table depth and permeability):

$$RMSE^j = \sqrt{\frac{\sum_1^n (\mathrm{Output\_}Y_i^j - \mathrm{True\_}Y_i^j)^2}{n}}, \tag{30}$$

where *j* denotes the corresponding numbers of different parameters (*j* = 1 for dwt, and *j* = 2 - 5 for k1-4 respectively). *n* is the number of samples for training the network, which is 5000 in this case. $\mathrm{Output\_}Y_i^j$ and $\mathrm{True\_}Y_i^j$ are the reconstructed and true output of the *j*th parameter of the *i*th sample. Here, we separately present the RMSEs of different parameters since the output dataset indicate different properties and in different scales. The ranges of *P*, *Q* and *M* are [10:5:100], [10:5:100], and [10:10:500], respectively. The regularization coefficient is set to 10^{-8} (see Chen & Liu, 2017). The optimum sets of parameters for training models are given in Table 2. The RMSEs of water table depth can be limited to 0.034 m. The RMSEs of permeability of layer 1 are much higher than layers 2-4. In contrast with deep layers, the permeability of the top layer is easier to be directly investigated in situ. k2 and k3 reach their optimum under *P*=15, *Q*=10 and *M*=500, and correspondingly, the RMSEs for estimating the dwt and k4 are satisfactory with the same setting.

Table 2

RMSEs of training data set with different configurations of the BL model (bold numbers denote the corresponding minimum RMSEs)

Parameters of BL model			**RMSE of training models**				
P	*Q*	*M*	dwt (m)	k1 (D)	k2 (D)	k3 (D)	k4 (D)
100	100	500	**0.0210**	2.4174	0.1462	0.1899	0.1526
80	40	500	0.0271	**2.4090**	0.1713	0.2005	0.1644
15	10	500	0.0339	2.4274	**0.1415**	**0.1603**	0.1616
10	10	500	0.0336	2.4239	0.1473	0.1628	**0.1500**

As the parameters' estimation accuracy is the highest when the number of enhancement nodes (*M*) reaches the maximum in the search range, we expanded this range to search for an appropriate neural network. The neural network gets more complex structures with a large number of groups, mapping feature nodes, and enhancement nodes, which may empower the BL model to describe the approximate mapping relationship between the input and output data from the training data set. As shown in Figure 2b, M directly reflects the complexity of the connected matrix for linking the integration of the feature mapping layer and the enhancement layer with the output layer. To examine whether the RMSEs would be reduced by keeping increasing the enhancement nodes and fixing P = 15 and Q = 10, we display the RMSEs varying with the number of enhancement nodes (Figure 10). In addition, we utilized 500 untrained samples from the validation dataset to test the inverted performance with increasing M. Further, the measured data in practice ineluctably contain some noise. With the improvement of pre-and post-processing techniques on near-surface SE applications, the signal-to-noise ratio (SNR) can be achieved to 20 – 45 dB (Butler & Russel, 2003; Butler et al., 2007). Thereby, to account for the possible interferences from self-noise and background noise, we add 5% random noise of the mean amplitude of synthetic SESRs at each trace (SNR ≈ 26 dB) to the initial validation and testing datasets without noise contamination. Similar to the treatment of the training dataset, the RMSEs of the validation dataset are calculated by replacing the number of samples in Equation 30 to 500 and updating the corresponding output dataset. Slightly though, the RMSE set keeps decreasing with M increasing (Figures 10a, 10c, 10e, and 10g), which indicates the neural network has been adapted to the training data set. However, there are different trends shown in untrained samples (Figures 10b, 10d, 10f, and 10h).

The parameter estimation using untrained noisy data as input performs better when M is lower than 300 (Figures 10b, 10d, 10f, and 10h). The number of enhancement nodes of each parameter reaching a minimum RMSE is given in Table 3. To show the influence of chosen M on the inversion accuracy, we contrast the true and reconstructed models by inputting noisy MC-SESRs of the validation dataset under the BL neural networks trained by M = 50, 200, 500, and 1000, respectively. Taking the water table depth as an example to display (Figure 11), the majority of reconstructed models are visually closer to the true models with increasing M, but the RMSE increases when $M \geq 200$ (Figures 11c-d). The reconstructed permeability also presents a similar trend (see Figures S1-S3 of Supporting Information). It can be attributed to the large departure of a few estimations from the true models. Finally, to detect the dynamic water table, we choose M = 240 as the number of enhancement nodes to train the BL model.

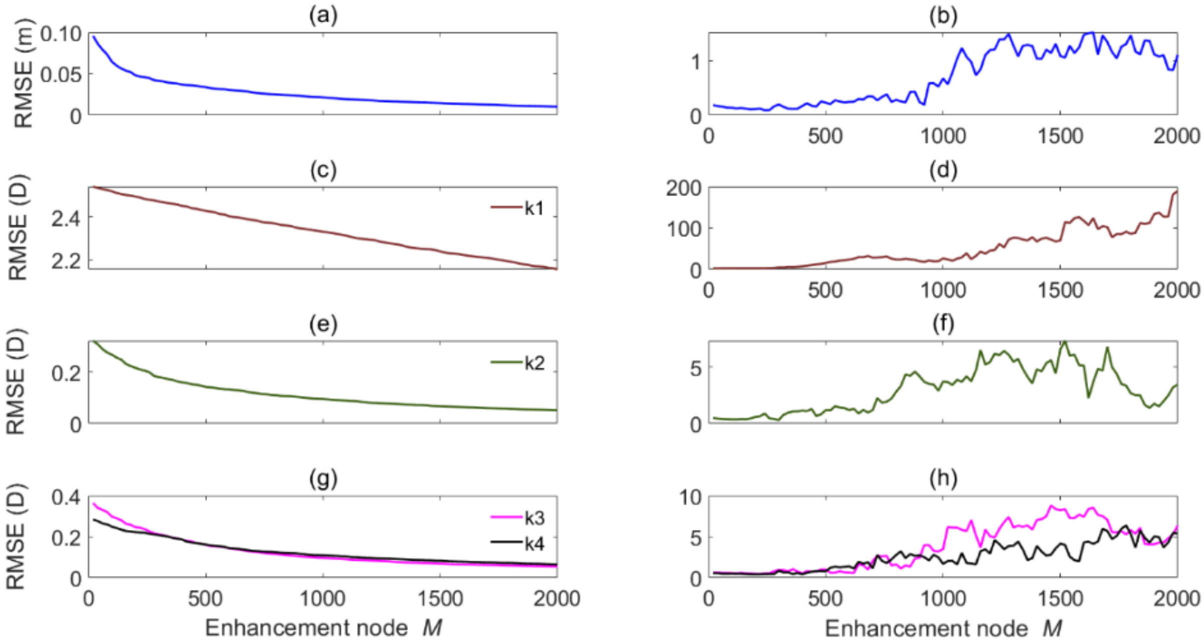

Figure 10. RMSEs of output data (a-b: water table depth, c-d: permeability of layer 1, e-f: permeability of layer 2, and g-h: permeability of layers 3-4) vary with the number of enhancement nodes (P=15, Q=10). Panels in the left column (a, c, e, g) represent the training data set and panels in the right column (b, d, f, h) represent the validation noisy dataset.

Table 3

RMSEs of validation data set with the optimum number of enhancement nodes (bold numbers denote the corresponding minimum RMSEs)

Enhancement node	**RMSE of validation models**				
M	dwt (m)	k1 (D)	k2 (D)	k3 (D)	k4 (D)
240	**0.0895**	2.7884	0.8879	0.5321	0.4339
20	0.1839	**2.6092**	0.4798	0.6212	0.5654
300	0.1945	4.5221	**0.3084**	0.9505	0.8540
220	0.1196	2.7551	0.6383	**0.4510**	0.4140
200	0.1117	2.8753	0.5839	0.4730	**0.4101**

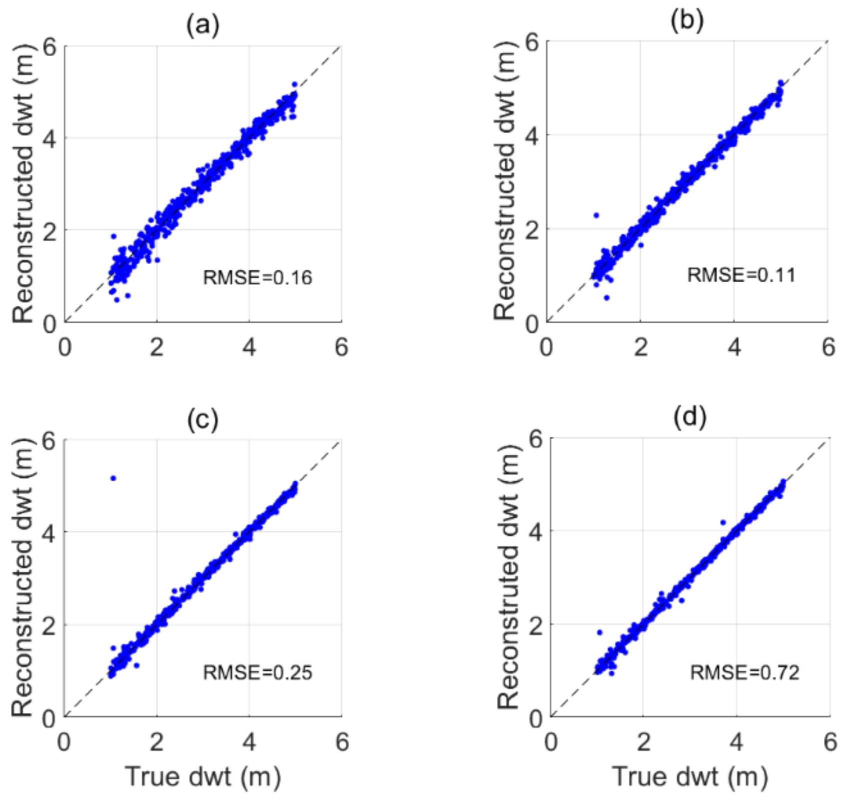

Figure 11. Comparisons of the true and reconstructed depth of water table (dwt) of the validation dataset with (a) M = 50, (b) M = 200, (c) M = 500, and (d) M = 1000

4.2. Comparisons of reconstructed and true models

After the 500 validation samples validated the BL model obtained by the 5000 training samples, we took the third step to attain MC-SESRs inversion. We applied this BL neural network configured by P=15, Q=10, and M=240 to invert the water table depth and permeability of 1000 testing samples with the same amount of noise contamination as the original testing MC-SESRs dataset. The testing dataset is independent of the training or validation datasets. The RMSEs of the testing dataset are calculated similarly to the validation dataset (Equation 30). The reconstructed depth of the water table has great consistency with corresponding true values (Figure 12a), whose RMSE is 0.09 m. The inversion results can nicely reconstruct the permeability of layer 2 (Figure 12c), whose RMSE is 0.46 D. the reconstructed permeability of layers 3 and 4 deviates more from true values than layer 2 (Figure 12d), while their RMSEs are acceptable (0.56 D and 0.43 D, respectively). Nevertheless, the permeability of the partially saturated layer 1 cannot be reconstructed, which concentrates around 5 D. It reflects that the SESRs data did not constrain the permeability of the unsaturated layer well since the low saturation makes a very low effective permeability to obtain a small SE coupling coefficient (Equation 11).

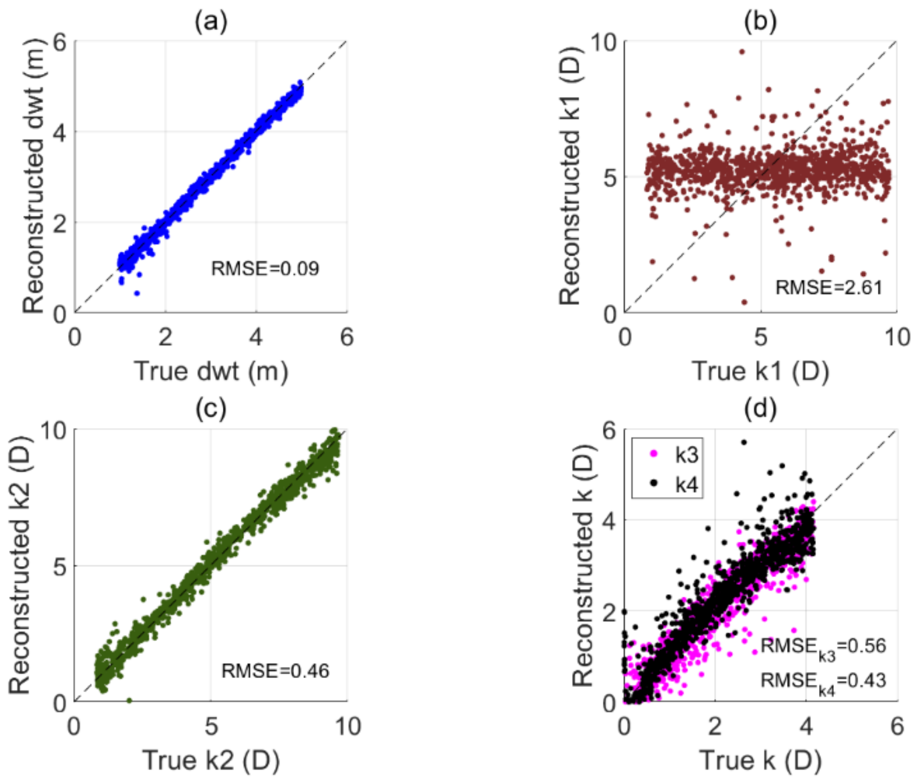

Figure 12. Comparisons of the true and reconstructed (a) depth of water table, (b) permeability of layer 1, (c) permeability of layer 2 and (d) permeability of layers 3-4 using noisy MC-SESRs data (SNR ≈ 26 dB).

Based on the settings of the basic test model, we used the SESRs data introduced in Section 3.3 to characterize variations in the water table depth. As the data uncertainty not only can originate from the noise but also possibly contains the errors of the model parameters, here, we assumed five-percent errors of dwt, permeability, and porosity included in the basic test model. Still, the data are assumed to be contaminated by five-percent random noise in the following tests. Meanwhile, as the sensitivity analysis of SESRs to the dwt in Section 3.3 shows, the short-offset SESRs are more sensitive than the long-offset SESRs to the variations of dwt, we test to apply the different number of channels to reconstruct the dynamic dwt. All 101 channels' or 26 short-offset channels' SESRs data used to invert the dwt can obtain comparable accuracy under five-percent errors in model parameters (Figure 13). This test indicates that we can reconstruct dynamic shallow dwt by using less short-offset MC-SESRs data. Since higher errors may occur in realistic measurements, we compare the inversion accuracy under five-percent, ten-percent, and twenty-percent errors in the pre-defined model using 26 short-offset channels' SESRs in Figure 14. The inverted water table depths are more deviated from the true values by enhancing errors. However, the overall inverted values are consistent with the true values with twenty-percent errors in the known model parameters, except for the result in September (Figure 14c).

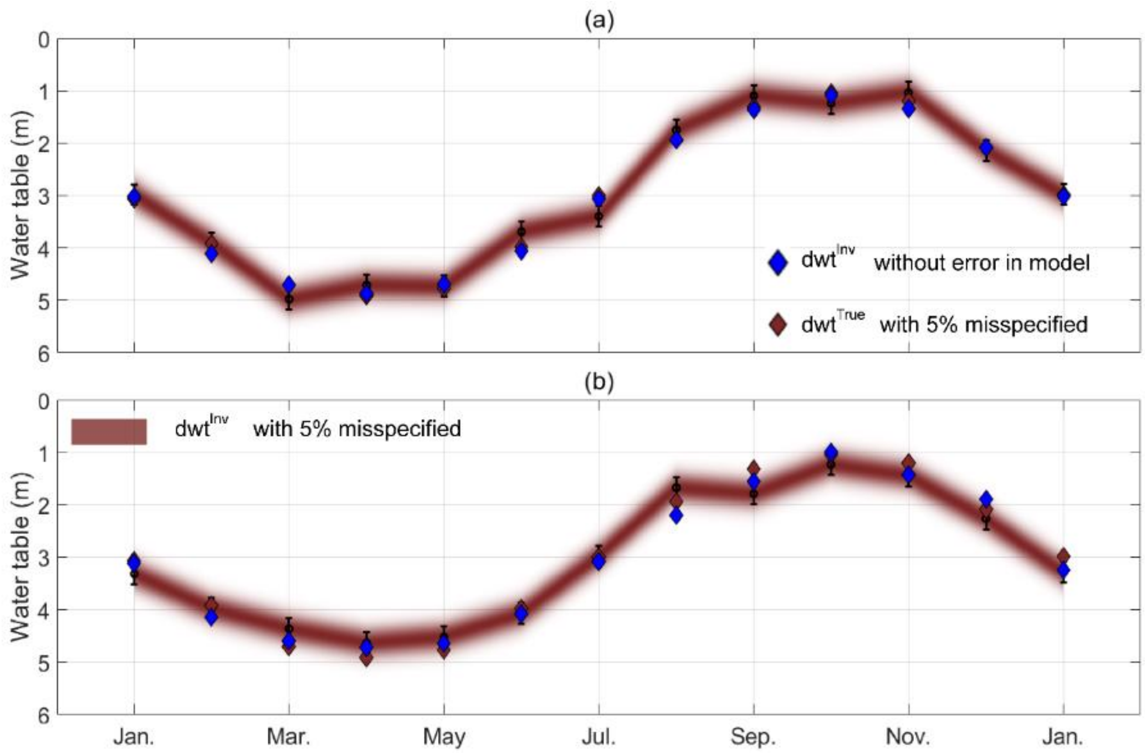

Figure 13. Detection of the water table depth using noisy MC-SESRs data collected from (a) 101 traces (5 - 105 m) and (b) 26 traces (5 - 30 m). The blue diamonds represent the inverted value without the model errors; The red diamonds represent the true values with 5%-misspecified errors in pre-defined model parameters; The circles represent the inverted values, whose misspecified levels are indicated by the shaded areas and error bars.

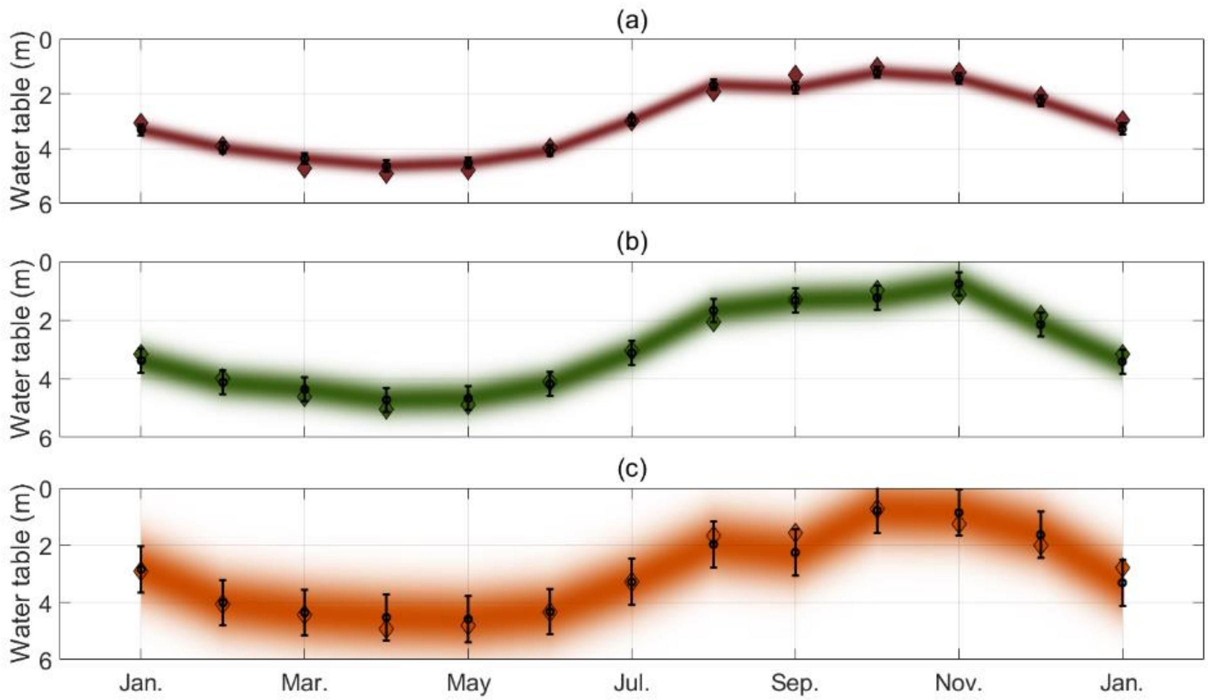

Figure 14. Detection of the water table depth using the noisy 26-channel SESRs data with misspecified errors of (a) 5%, (b) 10%, and (c) 20% in pre-defined model parameters. Diamonds represent the true values; The circles represent the inverted values, whose misspecified levels are indicated by the shaded areas and error bars.

As the absolute pressure head in the vadose zone is assumed to be the distance between its elevation and the water table level, the effective permeability and water saturation are calculated by the MVG model. We show that the true and the inverted permeabilities vary with time in Figure 15. The permeability can still be reconstructed in the time-lapse profiles (Figure 15a). The predicted accuracy is also reduced when errors added to the model are enhanced (Figures 15b and 15c). Particularly, the inverted errors of permeability increase in layer 4 due to the increasingly attenuated seismic and SE signals strength. The model parameters may be misspecified by larger errors, which causes lower inverted accuracy in deep layers due to the fragile signals.

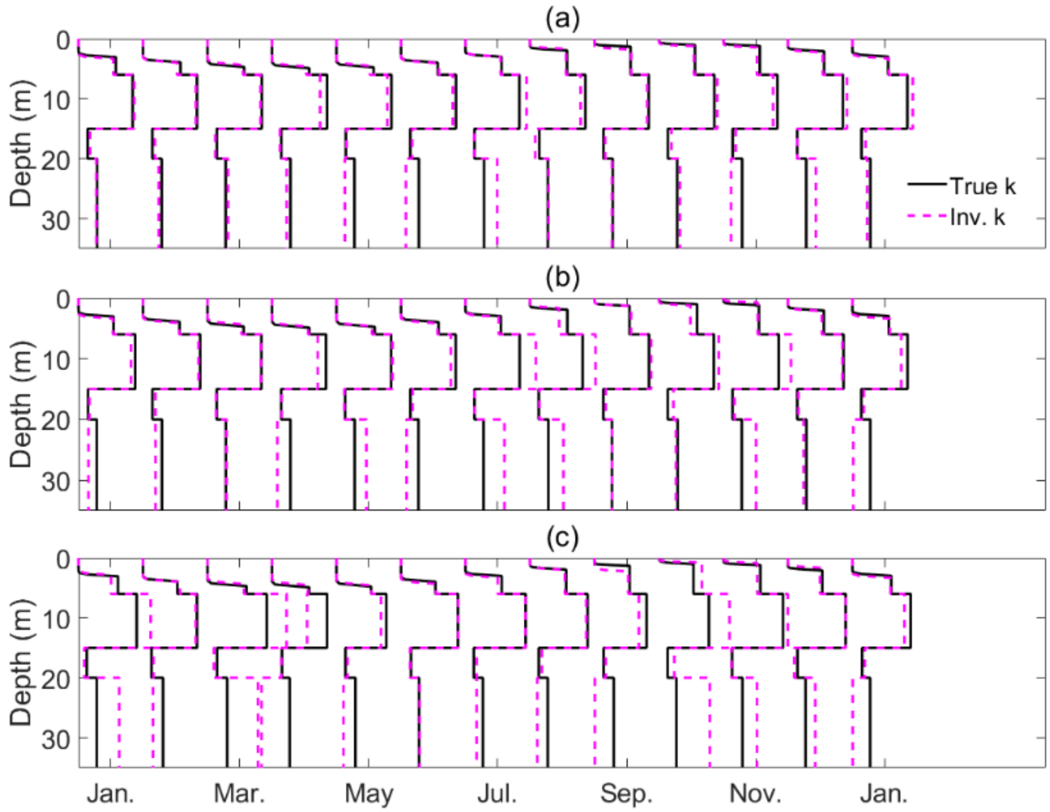

Figure 15. Comparison of true (black lines) and inverted (pink) permeability with the changing water table depth by accounting for errors of (a) 5%, (b) 10% and (c) 20% in pre-defined model parameters.

5. Discussion

To test the capability of this neural network in the presence of noise, we decrease the SNR to 20 dB, 16 dB, and 14 dB by considering different random noise levels (10%, 15%, and 20%) into synthetic MC-SESRs data. Based on the assumptions in Section 4.3, we attempt to use the SESRs data at different noise levels to detect the changing water table levels. As shown in Figure 16, the inverted accuracy is reduced when the noise is enhanced from 5% to 10% and more. In this case, the water table detection can be achieved at a 10% noise level when 26-channel SESR data (5 – 30 m) have been involved in the inversion (Figure 16a). This scenario can be improved by increasing the data by using more traces. The RMSE reaches 0.1671 m at a 20%-noise level when the used channels increase to 101. Correspondingly, the source-receiver offset ranges from 5 to 105 m (Figures 16b, 16d, and 16f). The inverse modeling may be able to perform well for stronger noise levels when the used MC-SESR data are sufficient. Note that the monitoring test in Section

4.2 discussed the influence of different levels of errors in model parameters (Figures 13-15). Ideally, although the water table and permeability changed with time and contained model perturbations, the well-trained network (Figure 2) can recover their true values for a specific site. Therefore, the inverted values are still close to the true values using 26-channel data with mixing the noise level of 5% (Figure 13). However, the porosity of each layer is also assumed to be misspecified. Thus, the increased errors in the pre-defined model decrease the inverted accuracy of the water table depth and permeability.

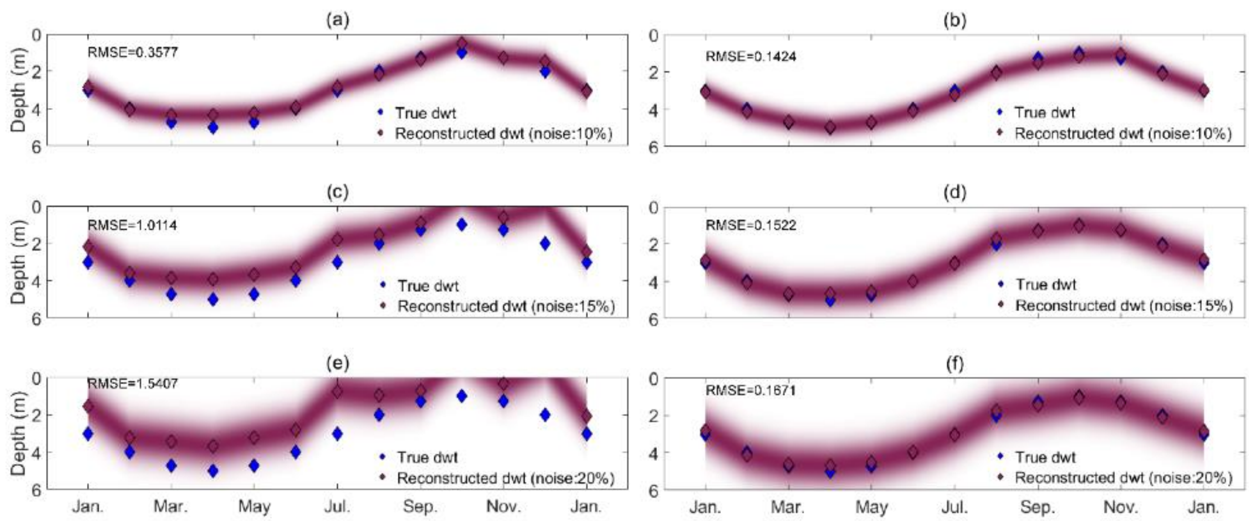

Figure 16. Comparison of true (blue) and predicted (purple) water table depth by adding (a-b) 10%, (c-d) 15% and (e-f) 20% random noise into data. The left panels (a, c, and e) use 26-channel SESRs data and the right panels (b, d, and f) use 101-channel SESRs data. The shaded areas indicate the misspecified levels.

As aforementioned sensitivity of permeability and water table depth in Sections 3.2-3.3, the SESRs at different source-receiver offsets respond to the variations of different layers. The number and locations of sensors used for inversion may affect the inverted results. We test the inverted RMSEs using MC-SESRs with different offsets by 1000 untrained random models. The interval distance of adjacent sensors is kept at 1 m. It starts from offset = 10 m, which means that MC-SESRs data obtained by 6 traces in the range of 5 – 10 m are used for inversion (see Section 2.3 $\mathbf{X}: \mathbf{SESR}_{5000\times36\times6}$). Figure 17 shows that the RMSEs dropped considerably when the used offsets increased to 30 m, but they continued reducing to a lesser extent. Generally, more SESRs data used for inversion should obtain higher inverted accuracy.

Picking a model to contrast the true with reconstructed parameters, the predicted permeability can reconstruct the effective permeability above the capillary fringe based on the water table estimation. However, the predicted saturated permeability of layer 1 deviates from its true value (Figure 18a). The inverted saturated permeability of the top layer poorly fits the true value embodied in the whole test set (Figure 12b). As the effective permeability drops considerably at low water saturations, the SE coupling coefficient is rather small. Thus, the information of the saturated permeability in layer 1 cannot be extracted by the mapping feature layer of input MC-SESRs data. The water table depth and permeability of layers 2-4 of the model are well estimated. Although the noisy MC-SESRs data for inversion are affected by disturbances (Figure 18c), the MC-SESRs data calculated by the predicted model (Figure 18d) well fit the synthetic MC-SESRs data (Figure 18b). The fitting errors concentrate in 10 – 25 m and low frequencies (~3 Hz) (Figure 18e). The inversion accuracy for this case is satisfactory by using data from 26 channels (~30 m) to train and invert the water table depth and permeability. One estimation with lower accuracy is presented in the Figure S4 of Supporting Information, whose modeling result from the inverted parameters can recover the overall shape and trend of the original data, but the maximum absolute difference is one order of magnitude larger than Figure 18e.

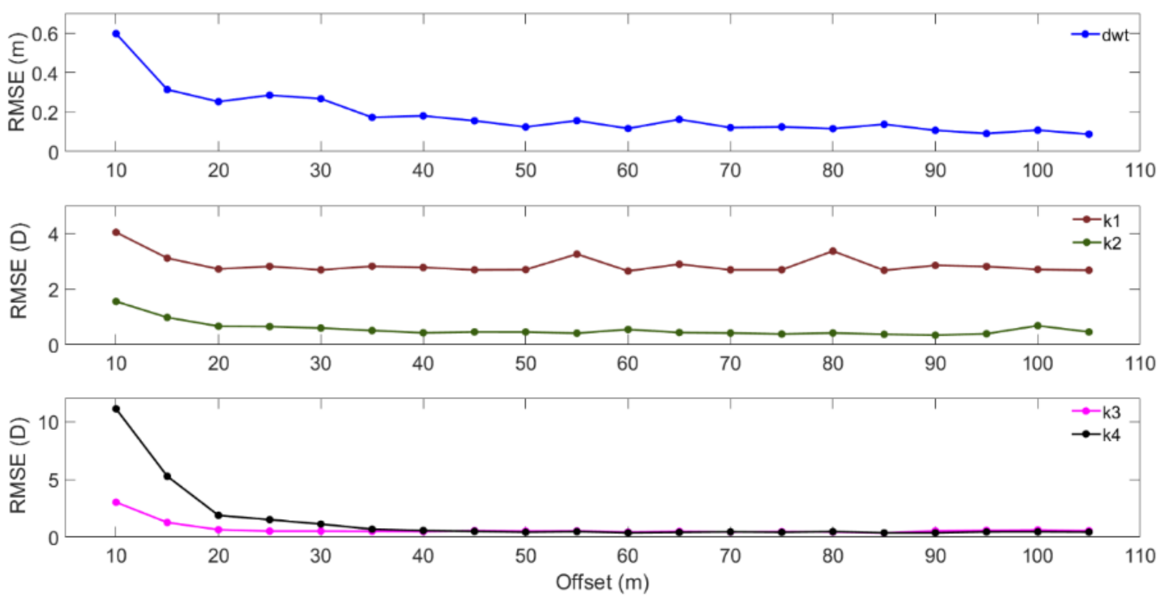

Figure 17. RMSEs between inverted and true models vary with the offset (SNR ≈ 26 dB). (a) water table depth, (b) permeability of layers 1-2 and (c) permeability of layers 3-4

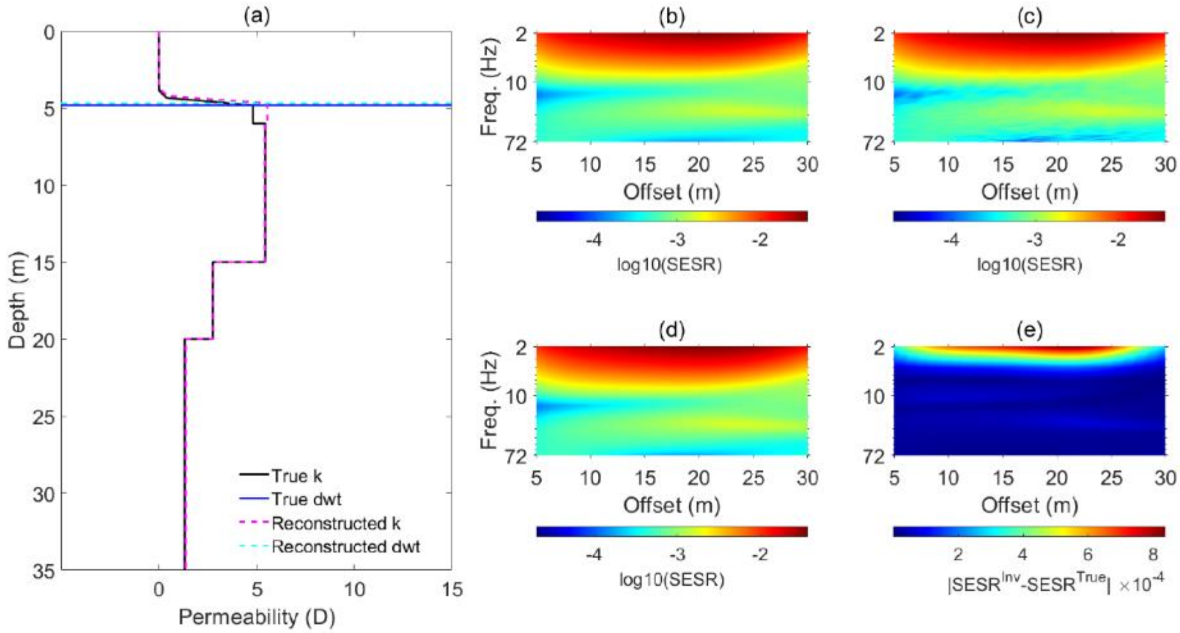

Figure 18. Comparisons of the true model and the reconstructed model using 26-channel SESR data. (a) The blue (solid) and cyan (dashed) lines represent the true and predicted water table depth, respectively. The black (solid) and pink (dashed) lines represent the true and reconstructed permeability, respectively. (b-d) display the 26-channel synthetic and noisy SESR data modeling by (b-c) the true model and (d) the inverted model. (e) shows SESRs difference between the data modeling by the true model and the inverted model.

6. Conclusions

In this paper, we propose using MC-SESRs to process multi-channel SE signals and seismic signals recorded at the ground surface. By analyzing the sensitivity of MC-SESRs to the water table depth and permeability, the results indicate that MC-SESRs data obtained by different offsets respond to the variations of different water table depths and permeability. Moreover, we introduce a simple and efficient BL approach to interpret MC-SESRs data to quantitatively infer the water table depth and permeability of layered-porous materials. As a type of non-invasive measurement, MC-SESRs obtained by surface observations can supplement traditional piezometer installations. It can be applied to rapidly and accurately detect the water table for a specific investigated field even though pre-defined model parameters are misspecified by 20%. This feature of monitoring the water table has potential applications for assessing groundwater storage and studying frost thawing and volcanic eruption. Nevertheless, as aforementioned, the dynamic effective excess charge density using the scaling factors by volumetric average and relaxation time suffers several limits as predictions, particularly at the pore scale. We suggest considering explicit frequency- and saturation-dependence in the future (Jougnot & Solazzi, 2021; Solazzi et al., 2022; Thanh et al., 2022).

Appendix A

Tables A1 and A2 list the acronyms as well as the notation and description of symbols used in the manuscript, respectively. The formulations of frequency-dependent (dynamic) and saturation-dependent parameters are summarized in Table A3.

Table A1. Acronyms and meaning

Acronyms	Meaning
SE	SeismoElectric
SESR	SeismoElectric Spectral Ratio
MC-SESR	Multi-Channel SeismoElectric Spectral Ratio
EDL	Electrical Double Layer
AVO	Amplitude variation Versus Offset
BL	Broad Learning
RVFLNN	Random Vector Functional Link Neural Network
EM	ElectroMagnetic
MVG	Mualem-van Genuchten
VG	van Genuchten
LAC GRTM	Luco-Apsel-Chen Generalized Reflection and Transmission Method
dwt	Water table depth

849 **Table A2**. Nomenclature of the Material Properties

Symbol	Unit	Description
ω	rad/s	Angular frequency
f	Hz	Frequency
ω_{t}	Hz	Angular transition frequency
θ_{c}	rad/s	The critical angle of evanescent electromagnetic waves
S_{w}	-	Water saturation
S_{wr}	-	Residual water saturation
S_{e}	-	Effective water saturation
σ^*	S/m	Complex electrical conductivity
σ_{w}	S/m	Electrical conductivity of pore water
σ_0	S/m	Static bulk electrical conductivity
$\mathbf{E}$	V/m	Electric field
$\mathbf{J}$	$\mathrm{A/m^2}$	Total current density
L^*	$\mathrm{A/m^2}$	Streaming cross-coupling coefficient
L_0^{sat}	$\mathrm{A/m^2}$	Streaming cross-coupling coefficient at the saturated condition in low frequency
$\hat{Q}_{\mathrm{v},0}^{\mathrm{sat}}$	$\mathrm{C/m^3}$	Saturated effective excess charge density in low frequency
$\hat{Q}_{\mathrm{v},0}$	$\mathrm{C/m^3}$	Effective excess charge density in low frequency
$\hat{Q}_{\mathrm{v}}^*$	$\mathrm{C/m^3}$	Complex effective excess charge density
CEC	C/kg	Cation exchange capacity
β_+	$\mathrm{m^2/sV}$	Mobility of the counterions in the diffuse layer
${\beta_+}^{\mathrm{sur}}$	$\mathrm{m^2/sV}$	Mobility of the counterions in the Stern layer
f_{Q}	-	Fraction of counterions in the Stern layer
${C_0}^{\mathrm{sat}}$	V/m	Streaming voltage coupling coefficient
C_{w}	mol/L	Salinity of pore water
F	-	Electrical formation factor
m	-	Cementation exponent of Archie's law
n	-	Saturation exponent of Archie's law
p_{f}	Pa	Pore-fluid pressure
ρ_{f}	$\mathrm{kg/m^3}$	Mass density of fluid
ρ_{s}	$\mathrm{kg/m^3}$	Mass density of solid
$\rho_{\mathrm{b}}^{\mathrm{sat}}$	$\mathrm{kg/m^3}$	Saturated bulk mass density
$\mathbf{u}_{\mathrm{s}}$	m/s	Averaging solid displacement
$\mathbf{u}_{\mathrm{f}}$	m/s	Averaging pore-fluid displacement
$\mathbf{w}$	m/s	Averaging filtration displacement
k^*	$\mathrm{m^2}$	Frequency-dependent permeability
k_0	-	Effective permeability in low frequency

k_0^{sat}	m^2	Saturated permeability in low frequency
ϕ	$\mathrm{m}^3/\mathrm{m}^3$	Porosity
α_{VG}	m^{-1}	Parameters of van Genuchten model
n_{VG}	-	Parameters of van Genuchten model
τ_{w}	-	Tortuosity
η_{w}	Pa·s	Dynamic viscosity of pore-water
α	-	Biot coefficient
α^{sat}	-	Saturated Biot coefficient
T	°C or K	Temperature
ε_0	F/m	Vacuum permittivity
κ_{w}	-	Dielectric constant of water
κ_{a}	-	Dielectric constant of air
κ_{s}	-	Dielectric constant of solid phase
K_{s}	Pa	Bulk modulus of solid phase
G	Pa	Frame shear modulus
K_{fr}	Pa	Frame bulk modulus
K_{w}	Pa	Bulk modulus of water
K_{a}	Pa	Bulk modulus of air
K_{G}	Pa	Undrained bulk modulus
C	Pa	Biot modulus
M	Pa	Biot modulus

850 **Table A3.** Frequency- and saturation-dependent parameters and corresponding formulations

Parameter	**Unit**	**Expression**	**References**
Angular transition frequency $\omega_{\mathrm{t}}(S_{\mathrm{w}})$	Hz	$\dfrac{\eta_{\mathrm{w}}\phi S_{\mathrm{w}}}{\rho_{\mathrm{w}}k_0(S_{\mathrm{w}})\tau_{\mathrm{w}}(S_{\mathrm{w}})}$	Revil & Mahardika, 2013; Solazzi et al., 2020
Tortuosity $\tau_{\mathrm{w}}(S_{\mathrm{w}})$	-	$\phi F {S_{\mathrm{w}}}^{1-n}$	Revil & Jougnot, 2008; Jougnot et al., 2018
Dynamic permeability $k^*(\omega, S_{\mathrm{w}})$	-	$\dfrac{k_0(S_{\mathrm{w}})}{1-\dfrac{i\omega}{2\omega_{\mathrm{t}}}}$	Revil & Mahardika, 2013
Effective water saturation $S_{\mathrm{e}}(S_{\mathrm{w}})$	-	$\dfrac{S_{\mathrm{w}}-S_{\mathrm{wr}}}{1-S_{\mathrm{wr}}}$	

Quasi-static effective permeability $k_0(S_\mathrm{w})$	-	$k_0{}^{\mathrm{sat}} S_\mathrm{e}^{\frac{1}{2}} \left[1 - \left(1 - S_\mathrm{e}^{\frac{1}{m_\mathrm{VG}}}\right)^{m_\mathrm{VG}}\right]^2$ $m_\mathrm{VG} = 1 - n_\mathrm{VG}{}^{-1}$	Mualem, 1976; van Genuchten, 1980
Specific moisture capacity $C_\mathrm{m}(S_\mathrm{w})$	m^{-1}	$\dfrac{\alpha_\mathrm{VG} m_\mathrm{VG} \phi (1 - S_\mathrm{wr}) S_\mathrm{e}^{\frac{1}{m_\mathrm{VG}}} \left(1 - S_\mathrm{e}^{\frac{1}{m_\mathrm{VG}}}\right)^{m_\mathrm{VG}}}{1 - m_\mathrm{VG}}$	Richards, 1931; van Genuchten, 1980
Frequency-dependent effective excess charge density $\hat{Q}_\mathrm{v}{}^*(\omega, S_\mathrm{w})$	-	$\hat{Q}_{\mathrm{v},0}(S_\mathrm{w}) \sqrt{1 - \dfrac{i\omega}{\omega_\mathrm{t}}}$	Revil & Mahardika, 2013
Complex electrical conductivity $\sigma^*(\omega, S_\mathrm{w})$	S/m	$\dfrac{S_\mathrm{w}{}^n \sigma_\mathrm{w}}{F} + \sigma_\mathrm{sur}(S_\mathrm{w}) + i[\sigma_\mathrm{quad}(S_\mathrm{w}) - \omega \varepsilon_0 \kappa(S_\mathrm{w})]$	Revil et al., 2015
Effective surface conductivity $\sigma_\mathrm{sur}(S_\mathrm{w})$	S/m	$\dfrac{2}{3} m \dfrac{(F-1)}{F} S_\mathrm{w}{}^{n-1} \beta_+ (1 - f_\mathrm{Q}) \rho_\mathrm{s} CEC$	Revil, 2013; Revil & Mahardika, 2013
Effective quadrature conductivity $\sigma_\mathrm{quad}(S_\mathrm{w})$	S/m	$-\dfrac{2}{3} m \dfrac{(F-1)}{F} S_\mathrm{w}{}^{n-1} \beta_+{}^{\mathrm{sur}} f_\mathrm{Q} \rho_\mathrm{s} CEC$	Revil, 2013; Revil & Mahardika, 2013
Dielectric constant $\kappa(S_\mathrm{w})$	-	$\dfrac{(F-1)\kappa_\mathrm{s} + S_\mathrm{w}{}^n \kappa_\mathrm{w} + (1 - S_\mathrm{w}{}^n)\kappa_\mathrm{a}}{F}$	Linde et al., 2006
Biot coefficient $\alpha(S_\mathrm{w})$	-	$\dfrac{S_\mathrm{w} - S_\mathrm{wr}}{1 - S_\mathrm{wr}} \alpha^{\mathrm{sat}}$	Revil & Mahardika, 2013
Mass density of fluid $\rho_\mathrm{f}(S_\mathrm{w})$	$\mathrm{kg/m^3}$	$S_\mathrm{w} \rho_\mathrm{w} + (1 - S_\mathrm{w}) \rho_a$	
Bulk modulus of fluid K_f	Pa	$\dfrac{1}{\dfrac{S_\mathrm{w}}{K_\mathrm{w}} + \dfrac{1 - S_\mathrm{w}}{K_a}}$	

851

Acknowledgments

Kaiyan Hu thanks the financial support of the National Natural Science Foundation of China (Grant No. 42104069), and the special fund for the scientific and technological development of Shenzhen guided by the central government of China (Grant No. 2021Szvup003). Hengxin Ren thanks the support from the National Natural Science Foundation of China (Grant No. 42022027), the Guangdong Provincial Key Laboratory of Geophysical High-resolution Imaging Technology (Grant No. 2022B1212010002), and the Shenzhen Science and Technology Program (Grant No. KQTD20170810111725321). The authors acknowledge the contributors and releasers of Broad Learning System codes (Chen & Liu, 2017) and the data set used in this work (Hu et al., 2022) for making their resources publicly available. We wish to thank editor Douglas Schmitt, associate editor Joel Sarout, and two anonymous reviewers for their constructive comments and suggestions, which greatly helped us to improve our manuscript.

Open Research

The data set and the main codes for inversion related to this manuscript can be found in the Hydrogeophysics Community of Zenodo (https://doi.org/10.5281/zenodo.7820571). The subroutines of the broad learning system can be found at https://broadlearning.ai/ (Chen & Liu, 2017). The used code of the peak-trough averaging algorithm is located at https://datadryad.org/stash/share/xXcw75yKN0M_C_MMcqYVKQxb-qAvGjf7ICPnahRBH4Y (Zheng et al., 2021).

References

Archie, G. E. (1942). The electrical resistivity log as an aid in determining some reservoir characteristics. *Transactions of the American Institute of Mining, Metallurgical and Petroleum Engineers*, *146*, 54–62. https://doi.org/10.2118/942054-G

Biot, M. A. (1956). Theory of propagation of elastic waves in a fluid saturated porous solid: I. low frequency range. *The Journal of the Acoustical Society of America*, *28*(2), 168–178. https://doi.org/10.1121/1.1908241

Biot, M. A. (1962a). Mechanics of deformation and acoustic propagation in porous media. *Journal of Applied Physic*, *33*, 1482-1498. https://doi.org/10.1063/1.1728759

Biot, M. A. (1962b). Generalized theory of acoustic propagation in porous dissipative media. *The Journal of the Acoustical Society of America*, *34*, 1254-1264. https://doi.org/10.1121/1.1918315

Bordes, C., Sénéchal, P., Barrière, J., Brito, D., Normandin, E., & Jougnot, D. (2015). Impact of water saturation on seismoelectric transfer functions: a laboratory study of coseismic phenomenon. *Geophysical Journal International*, *200*(3), 1317-1335. https://doi.org/10.1093/gji/ggu464

Butler, K. E., Russell, R. D., Kepic, A. W., & Maxwell, M. (1996). Measurement of the seismoelectric response from a shallow boundary. *Geophysics*, *61*, 1769–1778. https://doi.org/10.1190/1.1444093

Butler, K. E., Fleming, S. W., & Russell, R. D. (1999). Field test for linearity of seismoelectric conversions. *Canadian Journal of Exploration Geophysics*, *35*, 20-23.

Butler, K. E., & Russell, R. D. (2003). Cancellation of multiple harmonic noise series in geophysical records, *Geophysics*, *68*, 1083-1090. https://doi.org/10.1190/1.1581080

Butler, K. E., Dupuis, J. C., & Kepic, A. W. (2007). Improvements in signal-to-noise in seismoelectric acquisition. In Proceedings of exploration 07, Fifth Decennial International Conference on Mineral Exploration (pp. 1137–1141), Toronto.

Butler, K. E., Kulessa, B., & Pugin, A. J. (2018). Multimode seismoelectric phenomena generated using explosive and vibroseis sources. *Geophysical Journal International*, *213*(2), 836-850. https://doi.org/10.1093/gji/ggy017

Carsel, R. F., & Parrish, R. S. (1988). Developing joint probability distributions of soil water retention characteristics. *Water Resources Research*, *24*(5), 755-769. https://doi.org/10.1029/WR024i005p00755

Chen, C. P., & Liu, Z. (2017). Broad learning system: An effective and efficient incremental learning system without the need for deep architecture. *IEEE Transactions on Neural Networks and Learning Systems*, *29*(1), 10-24. https://doi.org/10.1109/TNNLS.2017.2716952

Dahlquist, G., & Björck, Å. (1974). *Numerical Methods*. Englewood Cliffs N. J., Prentice-Hall.

Devi, M. S., Garambois, S., Brito, D., Dietrich, M., Poydenot, V., & Bordes, C. (2018). A novel approach for seismoelectric measurements using multielectrode arrangements: II—Laboratory measurements. *Geophysical Journal International*, *214*(3), 1783–1799. https://doi.org/10.1093/gji/ggy251

Du, J., Vong, C. M., & Chen, C. P. (2020). Novel efficient RNN and LSTM-like architectures: Recurrent and gated broad learning systems and their applications for text classification. *IEEE Transactions on Cybernetics*, *51*(3), 1586-1597. https://doi.org/10.1109/TCYB.2020.2969705

Dukhin, S. S., & Derjaguin, B. V. (1974). Electrokinetic phenomena. In *Surface and Colloid Science*, (ed. E. Matijevic), *7*, 322. Wiley.

Dupuis, J. C., & Butler, K. E. (2006). Vertical seismoelectric profiling in a borehole penetrating glaciofluvial sediments. *Geophysical Research Letters*, *33*(16). https://doi.org/10.1029/2006GL026385

Dupuis, J. C., Butler, K. E., & Kepic, A. W. (2007). Seismoelectric imaging of the vadose zone of a sand aquifer. *Geophysics*, *72*, A81–A85. https://doi.org/10.1190/1.2773780

Dzieran, L., Thorwart, M., Rabbel, W., & Ritter, O. (2019). Quantifying interface responses with seismoelectric spectral ratios. *Geophysical Journal International*, *217*(1), 108-121. https://doi.org/10.1093/gji/ggz010

Dzieran, L., Thorwart, M., & Rabbel, W. (2020). Seismoelectric monitoring of aquifers using local seismicity—a feasibility study. *Geophysical Journal International*, *222*(2), 874-892. https://doi.org/10.1093/gji/ggaa206

Feng, S., Ren, W., Han, M., & Chen, Y. W. (2019). Robust manifold broad learning system for large-scale noisy chaotic time series prediction: A perturbation perspective. *Neural Networks*, *117*, 179-190. https://doi.org/10.1016/j.neunet.2019.05.009

Fitterman, D. V. (2015). Tools and techniques: Active-source electromagnetic methods. *Treatise on Geophysics (Second Edition)*, *11*, 295-333. https://doi.org/10.1016/B978-0-444-53802-4.00193-7

Garambois. S., & Dietrich, M. (2001). Seismoelectric wave conversions in porous media: Field measurements and transfer function analysis. *Geophysics*, *66*(5), 1417–1430. https://doi.org/10.1190/1.1487087

Garambois, S., & Dietrich, M. (2002). Full waveform numerical simulations of seismoelectromagnetic wave conversions in fluid-saturated stratified porous media. *Journal of Geophysical Research: Solid Earth*, *107*(B7), 1–19. https://doi.org/10.1029/2001JB000316

Ghanbarian, B., Hunt, A. G., Ewing, R. P., & Sahimi, M. (2013). Tortuosity in porous media: a critical review. *Soil Science Society of America Journal*, *77*(5), 1461–1477. https://doi.org/10.2136/sssaj2012.0435

Glover, P. W. J., & Jackson, M. D. (2010). Borehole electrokinetics. *The Leading Edge*, *29*(6), 724–728. https://doi.org/10.1190/1.3447786

Gong, X., Zhang, T., Chen, C. P., & Liu, Z. (2022). Research review for broad learning system: algorithms, theory, and applications. *IEEE Transactions on Cybernetics*, *52*(9), 8922-8950. https://doi.org/10.1109/TCYB.2021.3061094

Grobbe, N., & Slob, E. (2016). Seismo-electromagnetic thin-bed responses: Natural signal enhancements? *Journal of Geophysical Research: Solid Earth, 121*(4), 2460–2479. https://doi.org/10.1002/2015JB012381

Grobbe, N., Revil, A., Zhu, Z., & Slob, E. (Eds.). (2020). *Seismoelectric exploration: Theory, experiments, and applications* (Vol. 252). John Wiley & Sons.

Guarracino, L., & Jougnot, D. (2018). A physically based analytical model to describe effective excess charge for streaming potential generation in water saturated porous media. *Journal of Geophysical Research: Solid Earth*, *123*(1), 52-65. https://doi.org/10.1002/2017JB014873

Haartsen, M. W., & Pride, S. R. (1997). Electroseismic waves from point sources in layered media. *Journal of Geophysical Research: Solid Earth*, *102*(B11), 24745–24769. https://doi.org/10.1029/97JB02936

Haines, S. S., & Pride, S. R. (2006). Seismoelectric numerical modeling on a grid. *Geophysics*, *71*(6), N57-N65. https://doi.org/10.1190/1.2357789

Hu, H., & Gao, Y. (2011). Electromagnetic field generated by a finite fault due to electrokinetic effect. *Journal of Geophysical Research: Solid Earth*, *116*(B8), 1–14. https://doi.org/10.1029/2010JB007958

Hu, K., Jougnot, D., Huang, Q., Looms, M. C., & Linde, N. (2020). Advancing quantitative understanding of self- potential signatures in the critical zone through long-term monitoring. *Journal of Hydrology*, *585*, 124771. https://doi.org/10.1016/j.jhydrol.2020.124771

Hu, K., Ren, H., Huang, Q., Zeng, L., Butler, K. E., Jougnot, D., Linde, N., & Holliger, K. (2022). Dataset for "Water Table and Permeability Estimation from Multi-Channel Seismoelectric Spectral Ratios" [Data set]. Zenodo. https://doi.org/10.5281/zenodo.7820571

Hu, K., Huang, Q., Han, P., Han, Z., Yang, Z., Luo, Q., et al. (2023). A hydrochemical study of groundwater salinization in Qinzhou Bay, Guangxi, Southern China. *Earth and Space Science*, *10*, e2022EA002565. https://doi. org/10.1029/2022EA002565

Huang, Q. (2002). One possible generation mechanism of co-seismic electric signals, *Proceeding of the Japan Academy*, *Series B*, *78*(7), 173–178. https://doi.org/10.2183/pjab.78.173

Hunter, R. J. (1981). *Zeta Potential in Colloid Science: Principles and Applications.* Academic Press.

Jackson, M. D. (2010). Multiphase electrokinetic coupling: Insights into the impact of fluid and charge distribution at the pore scale from a bundle of capillary tubes model. *Journal of Geophysical Research: Solid Earth*, *115*(B7), 1-17. https://doi.org/10.1029/2009JB007092

Jardani, A., Revil, A., Boleve, A., Crespy, A., Dupont, J. P., Barrash, W., & Malama, B. (2007). Tomography of the Darcy velocity from self-potential measurements. *Geophysical Research Letters*, *34*(24), 1-6. https://doi.org/10.1029/2007GL031907

Jardani, A., Revil, A., Slob, E., & Söllner, W. (2010). Stochastic joint inversion of 2D seismic and seismoelectric signals in linear poroelastic materials: A numerical investigation. *Geophysics*, *75*(1), N19–N31. https://doi.org/10.1190/1.3279833

Jougnot, D., Linde, N., Revil, A., & Doussan, C. (2012). Derivation of soil-specific streaming potential electrical parameters from hydrodynamic characteristics of partially saturated soils. *Vadose Zone Journal, 11*(1). https://doi.org/10.2136/vzj2011.0086

Jougnot, D., Rubino, J. G., Carbajal, M. R., Linde, N., & Holliger, K. (2013). Seismoelectric effects due to mesoscopic heterogeneities. *Geophysical Research Letters*, *40*(10), 2033-2037. https://doi.org/10.1002/grl.50472

Jougnot, D., Jiménez-Martínez, J., Legendre, R., Le Borgne, T., Méheust, Y., & Linde, N. (2018). Impact of small-scale saline tracer heterogeneity on electrical resistivity monitoring in fully and partially saturated porous media: Insights from geoelectrical milli-fluidic experiments. *Advances in Water Resources*, *113*, 295-309. https://doi.org/10.1016/j.advwatres.2018.01.014

Jougnot, D., Roubinet, D., Guarracino, L., & Maineult, A. (2020). Modeling streaming potential in porous and fractured media, description and benefits of the effective excess charge density approach. *In Advances in modeling and interpretation in near surface geophysics* (pp. 61-96). Springer, Cham.

Jougnot, D., & Solazzi, S. G. (2021). Predicting the frequency-dependent effective excess charge density: A new upscaling approach for seismoelectric modeling. *Geophysics, 86*(5), WB77-WB86. https://doi.org/10.1190/geo2020-0524.1

Jouniaux, L., & Zyserman, F. (2016). A review on electrokinetically induced seismo-electrics, electro-seismics, and seismo-magnetics for earth sciences. *Solid Earth*, *7*(1), 249-284. https://doi.org/10.5194/se-7-249-2016

Knight, R. J., & Endres, A. L. (2005). An introduction to rock physics principles for near-surface geophysics. In: Butler D. K. (Ed.), *Near Surface Geophysics, Part 1: Concepts and Fundamentals*. Society of Exploration Geophysicists, *13*, p. 31-70.

Linde, N., Binley, A., Tryggvason, A., Pedersen, L. B., & Revil, A. (2006). Improved hydrogeophysical characterization using joint inversion of cross-hole electrical resistance and ground-penetrating radar traveltime data. *Water Resources Research*, *42*(11), W12404. https://doi.org/10.1029/2006WR005131

Linde, N., Jougnot, D., Revil, A., Matthai, S. K., Arora, T., Renard, D., & Doussan, C. (2007a). Streaming current generation in two-phase flow conditions. *Geophysical Research Letter*, *34*(3), L03306. https://doi.org/10.1029/2006GL028878

Linde, N., Revil, A., Bolève, A., Dagès, C., Castermant, J., Suski, B., & Voltz, M. (2007b). Estimation of the water table throughout a catchment using self-potential and piezometric data in a Bayesian framework. *Journal of Hydrology*, *334*, 89–99. https://doi.org/10. 1016/j.jhydrol.2006.09.027

Mao, S., Lecointre, A., van der Hilst, R. D., & Campillo, M. (2022). Space-time monitoring of groundwater fluctuations with passive seismic interferometry. *Nature Communications*, *13*, 4643. https://doi.org/10.1038/s41467-022-32194-3

Mikhailov, O. V., Haartsen, M. W., & Toksöz, M. N. (1997). Electroseismic investigation of the shallow subsurface: Field measurements and numerical modeling. *Geophysics*, *62*, 97–105. https://doi.org/10.1190/1.1444150

Monachesi, L. B., Zyserman, F. I., & Jouniaux, L. (2018). An analytical solution to assess the SH seismoelectric response of the vadose zone. *Geophysical Journal International*, *213*(3), 1999–2019. https://doi.org/10.1093/gji/ggy101

Mualem, Y. (1976). A new model for predicting the hydraulic conductivity of unsaturated porous media, *Water Resources Research*, *12*(3), 513–522. https://doi.org/10.1029/WR012i003p00513

Niu, Q., & Zhang, C. (2019). Permeability prediction in rocksexperiencing mineral precipitation anddissolution: A numerical study. *Water Resources Research*, *55*(4), 3107–3121. https://doi.org/10.1029/2018WR024174

Pao, Y. H., Park, G. H. & Sobajic, D. J. (1994). Learning and generalization characteristics of the random vector functional-link net, *Neurocomputing*, *6*(2), 163–180. https://doi.org/10.1016/0925-2312(94)90053-1

Pride, S. (1994). Governing equations for the coupled electromagnetics and acoustics of porous media. *Physical Review B*, *50*(21), 15678. https://doi.org/10.1103/PhysRevB.50.15678

Pride, S. R., & Haartsen, M. W. (1996). Electroseismic wave properties. *The Journal of the Acoustical Society of America*, *100*, 1301–1315. https://doi.org/10.1121/1.416018

Pride, S. R., & Garambois, S. (2002). The role of Biot slow waves in electroseismic wave phenomena. *The Journal of the Acoustical Society of America*, *111*, 697–706. https://doi.org/10.1121/1.1436066

Ren, H., Huang, Q., & Chen, X. (2007). Numerical simulation of seismoelectromagnetic waves in layered porous media. In *Paper Presented at Proceeding of the 8th China International Geo-Electromagnetic Workshop*.

Rabbel, W., Iwanowski Strahser, K., Strahser, M., Dzieran, L., & Thorwart, M. (2020). Seismoelectric field measurements in unconsolidated sediments in comparison with other methods of near surface prospecting. In: Grobbe, N., Revil, A., Zhu, Z., & Slob, - E. (Eds.), *Seismoelectric exploration: Theory, experiments, and applications*, American Geophysical Union Monograph Vol. 252, John Wiley & Sons, p. 347-363.

Ren, H., Huang, Q. & Chen, X. (2010). A new numerical technique for simulating the coupled seismic and electromagnetic waves in layered porous media, *Earthquake Science*, *23*(2), 167–176. https://doi.org/10.1007/s11589-009-0071-9

Ren, H., Huang, Q., & Chen, X. (2016a). Existence of evanescent electromagnetic waves resulting from seismoelectric conversion at a solid–porous interface. *Geophysical Journal International*, *204*(1), 147-166. https://doi.org/10.1093/gji/ggv400

Ren, H., Huang, Q., & Chen, X. (2016b). Numerical simulation of seismo-electromagnetic fields associated with a fault in a porous medium. *Geophysical Journal International*, *206*, 205–220. https://doi.org/10.1093/gji/ggw144

Ren, H., Huang, Q., & Chen, X. (2018). Quantitative understanding on the amplitude decay characteristic of the evanescent electromagnetic waves generated by seismoelectric conversion. *Pure and Applied Geophysics*, *175*(8), 2853-2879. https://doi.org/10.1007/s00024-018-1823-z

Revil, A., & Cerepi, A. (2004). Streaming potentials in two-phase flow conditions. *Geophysical Research Letters*, *31*(11). https://doi.org/10.1029/2004GL020140

Revil, A., & Linde, N. (2006). Chemico-electromechanical coupling in microporous media. *Journal of Colloid and Interface Science*, *302*(2), 682-694. https://doi.org/10.1016/j.jcis.2006.06.051

Revil, A., Linde, N., Cerepi, A., Jougnot, D., Matthäi, S., & Finsterle, S. (2007). Electrokinetic coupling in unsaturated porous media. *Journal of Colloid & Interface Science, 313*(1), 315-327. https://doi.org/10.1016/j.jcis.2007.03.037

Revil A., & Jougnot D. (2008). Diffusion of ions in unsaturated porous materials. *Journal of Colloid & Interface Science, 319*(1), 226-235. https://doi.org/10.1016/j.jcis.2007.10.041

Revil, A., Karaoulis, M., Johnson, T., & Kemna, A. (2012). Some low-frequency electrical methods for subsurface characterization and monitoring in hydrogeology. *Hydrogeology Journal*, *20*(4), 617–658. https://doi.org/10.1007/s10040-011-0819-x

Revil, A. (2013). Effective conductivity and permittivity of unsaturated porous materials in the frequency range 1 mHz–1GHz. *Water Resources Research*, *49*(1), 306-327. https://doi.org/10.1029/2012WR012700

Revil, A., & Jardani, A. (2013). *The self-potential method: Theory and applications in environmental geosciences*. Cambridge University Press.

Revil, A., & Mahardika, H. (2013). Coupled hydromechanical and electromagnetic disturbances in unsaturated porous materials. *Water Resources Research, 49*(2), 744-766. https://doi.org/10.1002/wrcr.20092

Revil, A., Jardani, A., Sava, P., & Haas, A. (2015). *The Seismoelectric Method: Theory and Applications*. John Wiley & Sons.

Richards, L. A. (1931). Capillary conduction of liquids through porous media, *Physics*, *1*, 318 – 333. https://doi.org/10.1063/1.1745010

Rosas-Carbajal, M., Jougnot, D., Rubino, J. G, Monachesi, L., Linde, N., & Holliger, K. (2020). Seismoelectric signals produced by mesoscopic heterogeneities: spectroscopic analysis of fractured media. In: Grobbe, N., Revil, A., Zhu, Z., & Slob, - E. (Eds.), *Seismoelectric exploration: Theory, experiments, and applications*, American Geophysical Union Monograph Vol. 252, John Wiley & Sons, p. 269-287.

Rutherford, S. R., & Williams, R. H. (1989). Amplitude-versus-offset variations in gas sands. *Geophysics*, *54*(6), 680-688. https://doi.org/10.1190/1.1442696

Solazzi, S. G., Rubino, J. G., Jougnot, D., & Holliger, K. (2020). Dynamic permeability functions for partially saturated porous media. *Geophysical Journal International*, *221*(2), 1182-1189. https://doi.org/10.1093/gji/ggaa068

Sen, P.N., & Goode, P. A. (1992). Influence of temperature on electrical conductivity on shaly sands. *Geophysics*, *57*, 89–96. https://doi.org/10.1190/1.1443191

Solazzi, S. G., Bodet, L., Holliger, K., & Jougnot, D. (2021). Surface-wave dispersion in partially saturated soils: The role of capillary forces. *Journal of Geophysical Research: Solid Earth*, *126*, e2021JB022074. https://doi.org/10.1029/2021JB022074

Solazzi, S.G., Thanh. L.D., Hu, K., & Jougnot, D. (2022). Modeling the frequency-dependent effective excess charge density in partially saturated porous media. *Journal of Geophysical Research: Solid Earth*, *127*(11): e2022JB024994. https://doi.org/10.1029/2022JB024994

Soldi, M., Jougnot, D., & Guarracino, L. (2019). An analytical effective excess charge density model to predict the streaming potential generated by unsaturated flow. *Geophysical Journal International*, *216*(1), 380-394. https://doi.org/10.1093/gji/ggy391

Soldi, M., Guarracino, L., & Jougnot, D. (2020). An effective excess charge model to describe hysteresis effects on streaming potential. *Journal of Hydrology*, *588*, 124949. https://doi.org/10.1016/j.jhydrol.2020.124949

Thanh, L. D., Jougnot, D., Solazzi, S. G., Van Nghia, N., & Van Do, P. (2022). Dynamic streaming potential coupling coefficient in porous media with different pore size distributions. *Geophysical Journal International*, *229*(1), 720-735, https://doi.org/10.1093/gji/ggab491

Thompson, A. H., & Gist, G. A. (1993). Geophysical applications of electrokinetic conversion. *The Leading Edge*, *12*, 1169–1173. https://doi.org/10.1190/1.1436931

van Genuchten, M. T. (1980). A closed-form equation for predicting the hydraulic conductivity of unsaturated soils. *Soil Science Society of America Journal*, *44*(5), 892-898. https://doi.org/10.2136/sssaj1980.03615995004400050002x

Wang, J., Zhu, Z., Gao, Y., Morgan, F. D., & Hu, H. (2020). Measurements of the seismoelectric responses in a synthetic porous rock. *Geophysical Journal International*, *222*(1), 436-448. https://doi.org/10.1093/gji/ggaa174

Warden, S., Garambois, S., Jouniaux, L., Brito, D., Sailhac, P., & Bordes, C. (2013). Seismoelectric wave propagation numerical modelling in partially saturated materials. *Geophysical Journal International*, *194*(3), 1498-1513. https://doi.org/10.1093/gji/ggt198

Wu, S., Huang, Q., & Zhao, L. (2021). Conventional neural network inversion of airborne transient electromagnetic data. *Geophysical Prospecting, 69*(8-9), 1761-1772. https://doi.org/10.1111/1365-2478.13136

Yang, X. H., Han, P., Yang, Z., Miao, M., Sun, Y. C., & Chen, X. (2022). Broad learning framework for search space design in Rayleigh wave inversion. *IEEE Transactions on Geoscience and Remote Sensing*, *60*, 1-17. Article no. 4512617. https://doi.org/10.1109/TGRS.2022.3208616

Yang, X. H., Han, P., Yang, Z., & Chen, X. (2023). Two-stage broad learning inversion framework for shear-wave velocity estimation. *Geophysics*, *88*, WA219-WA237. https://doi.org/10.1190/geo2022-0060.1

Yuan, S., Ren, H., Huang, Q., Zheng, X.-Z., & Chen, X. (2021). Refining higher modes of Rayleigh waves using seismoelectric signals excited by a weight-drop source: study from numerical simulation aspect. *Journal of Geophysical Research: Solid Earth*, *126*(5), e2020JB021336. https://doi.org/10.1029/2020JB021336

Zhang, H.-M., Chen, X.-F., & Chang, S. (2001). Peak-trough averaging method and its applications to calculation of synthetic seismograms with shallow focuses. *Chinese Journal of Geophysics*, *44*(6), 791–799. https://doi.org/10.1002/cjg2.201

Zhang, H.-M., Chen, X.-F., & Chang, S. (2003). An efficient numerical method for computing synthetic seismograms for a layered half-space with sources and receivers at close or same depths. In Seismic motion, lithospheric structures, earthquake and volcanic sources: The Keiiti Aki volume (pp. 467–486). Springer. https://doi.org/10.1007/PL00012546

Zheng, X.-Z., Ren, H., Butler, K. E., Zhang, H., Sun, Y.-C., Zhang, W., et al. (2021). Seismoelectric and electroseismic modeling in stratified porous media with a shallow or ground surface source. *Journal of Geophysical Research: Solid Earth*, *126*(9), e2021JB021950. https://doi.org/10.1029/2021JB021950

Zhu, Z., & Toksöz, M. N. (2013). Experimental measurements of the streaming potential and seismoelectric conversion in Berea sandstone. *Geophysical Prospecting*, *61*(3), 688-700. https://doi.org/10.1111/j.1365-2478.2012.01110.x

Zyserman, F. I., Monachesi, L. B., & Jouniaux, L. (2017). Dependence of shear wave seismoelectrics on soil textures: a numerical study in the vadose zone. *Geophysical Journal International*, *208*(2), 918-935. https://doi.org/10.1093/gji/ggw431